LLNL-JRNL-439512

LAWRENCE LIVERMORE NATIONAL LABORATORY

Analysis of turbulent transport and mixing in transitional Rayleigh-Taylor unstable flow using direct numerical simulation data

O. Schilling

July 1, 2010

Physics of Fluids

Analysis of turbulent transport and mixing in transitional Rayleigh–Taylor unstable flow using direct numerical simulation data

Oleg Schilling*
Lawrence Livermore National Laboratory, Livermore, California 94550, USA

Nicholas J. Mueschke†
Department of Mechanical Engineering, Texas A&M University, College Station, Texas 77843, USA
(Dated: June 16, 2010)

Data from a $1152 \times 760 \times 1280$ direct numerical simulation (DNS) [Mueschke and Schilling, Phys. Fluids **21**, 014106 (2009)] of a transitional Rayleigh–Taylor mixing layer modeled after a small Atwood number water channel experiment is used to comprehensively investigate the structure of mean and turbulent transport and mixing. The simulation had physical parameters and initial conditions approximating those in the experiment. The budgets of the mean vertical momentum, heavy-fluid mass fraction, turbulent kinetic energy, turbulent kinetic energy dissipation rate, heavy-fluid mass fraction variance, and heavy-fluid mass fraction variance dissipation rate equations are constructed using Reynolds averaging applied to the DNS data. The relative importance of mean and turbulent production, turbulent dissipation and destruction, and turbulent transport are investigated as a function of Reynolds number and along the spanwise extent of the mixing layer to provide insight into the dynamics of the flow not presently available from experiments. The analysis of the budgets supports the assumption for small Atwood number, Rayleigh–Taylor driven flows that the principal transport mechanisms in the flow are buoyancy production, turbulent production, turbulent dissipation, and turbulent diffusion (shear and mean field production are negligible). As the Reynolds number increases, the turbulent production in the turbulent kinetic energy dissipation rate equation becomes the dominant production term, while the buoyancy production plateaus. Distinctions between momentum and scalar transport are also noted, where the turbulent kinetic energy and its dissipation rate both grow in time and are peaked near the center plane of the mixing layer, while the heavy-fluid mass fraction variance and its dissipation rate initially grow and then begin to decrease as the mixing progresses and reduces density fluctuations. All terms in the transport equations generally grow or decay, with no qualitative change in their profile, except for the pressure flux contribution to the total turbulent kinetic energy flux, which changes sign early in time (a countergradient effect). The production-to-dissipation ratios corresponding to the turbulent kinetic energy and heavy-fluid mass fraction variance are large and vary strongly at small evolution times, decrease with time, and nearly asymptote as the flow enters a self-similar regime. The late-time turbulent kinetic energy production-to-dissipation ratio is larger than observed in shear-driven turbulent flows. Order of magnitude estimates of the terms in the transport equations are shown to be consistent with the DNS at late time, and also confirm both the dominant terms and their evolutionary behavior. These results are useful for identifying the dynamically important terms requiring closure, and assessing the accuracy of the predictions of Reynolds-averaged Navier–Stokes and large-eddy simulation models of turbulent transport and mixing in transitional Rayleigh–Taylor instability-generated flow.

PACS numbers: 47.20.-k, 47.20.Ma, 47.27.-i, 47.27.Cn, 47.27.E-, 47.27.ek, 47.27.wj

I. INTRODUCTION

Modeling the statistical properties of Rayleigh–Taylor instability-induced mixing is of fundamental fluid mechanics interest, as well as of interest to the hydrodynamic modeling of inertial confinement fusion and astrophysics. The analysis of Rayleigh–Taylor instability-driven flows is complicated by variable density, nonstationary, anisotropy, and inhomogeneity. While large-scale properties of Rayleigh–Taylor mixing layers have been measured in experiments and simulations, there has been comparatively less effort to investigate small-scale properties and turbulence statistics. The present work investigates the structure of the transport equations of the lowest-order variances and their corresponding dissipation rates during the growth and transition to turbulence of a Rayleigh–Taylor mixing layer using direct numerical simulation (DNS) data.[1] This analysis is useful for quantitatively assessing the predictions of Reynolds-averaged Navier–Stokes (RANS) and large-eddy simulation (LES) models of Rayleigh–Taylor turbulence *a priori* or *a posteriori*, and for guiding further development and validation of models. Order of magnitude estimates of the terms in the transport equations are shown to be consistent with the numerical findings, and confirm the

*Author to whom correspondence should be addressed. Electronic mail: schilling1@llnl.gov.
†Present address: Southwest Research Institute, San Antonio, Texas 78238.

important terms and their evolutionary behavior.

Experiments in a water channel[2–8] and a gas channel[9,10] at Texas A&M University have measured time-averaged and instantaneous quantities relevant to modeling Rayleigh–Taylor instability-induced mixing using thermocouple measurements, particle-image velocimetry, planar laser-induced fluorescence, and hot- or cold-wire anemometry. Quantities obtained from these experiments include the bubble front width $h_b(t)$ and self-similar growth parameter α_b, the molecular mixing parameter $\theta(t)$ on the center plane of the mixing layer, velocity variances, one-dimensional vertical velocity and density variance spectra, the density–velocity correlation, two-point correlations, probability distributions, and conditional statistics. While these measurements comprise the most complete body of experimental data on Rayleigh–Taylor flow over a wide Atwood number range ($\sim 10^{-3}$–0.6), this data is still insufficient to fully constrain Reynolds-averaged transport and mixing models for such flows. This, coupled with the observation that nearly all simulations of Rayleigh–Taylor flow either used monotone-integrated large-eddy simulation (MILES) or DNS with idealized isotropic initial conditions, motivated the DNS of the water channel experiment and the current investigation. The DNS was validated by comparing results with available experimental measurements,[1] and additional quantities not measured were computed and interpreted.[11] Distinct from other investigations of Rayleigh–Taylor flow, this flow field is representative of the conditions in a physical experiment. The present study provides terms in the transport equations that have not been measured experimentally and interprets their physical behavior.

Rayleigh–Taylor turbulent mixing is examined here by evaluating mean and turbulent transport equation budgets to quantify the relative importance of different processes during the nonlinear and early turbulent stages of evolution. As these equations form the basis of RANS models, understanding their structure during the flow evolution provides information for further theoretical development and assessment of the predictive capabilities of such models. The turbulent kinetic energy $\widetilde{E''}$, turbulent kinetic energy dissipation rate $\overline{\epsilon'}$, heavy-fluid mass fraction variance $\widetilde{m_1''^2}$, and heavy-fluid mass fraction variance dissipation rate $\widetilde{\chi''}$ equation budgets are considered. Examination of the last two equations addresses scalar transport and mixing in Rayleigh–Taylor flow. The current study cannot be performed using MILES or LES, as neither fully resolve the flow at the viscous and diffusive scales or provide direct measures of turbulent kinetic energy dissipation. Furthermore, correlations of products of gradients of fluctuating fields arising in the transport equations cannot be easily or accurately measured.

This paper is organized as follows. The DNS dataset is described in Sec. II. The structure of the mean flow, mechanical turbulence, and scalar turbulence is discussed in Sec. III, IV, and V, respectively, at different evolution times. The production-to-dissipation (or destruction) ratios are discussed in Sec. VI. Finally, a summary of the results of this study and conclusions are given in Sec. VII. The turbulent fluxes are considered in Appendix A, orders of magnitude of the terms in the transport equations are estimated in Appendix B, and the turbulent transport equations describing small Atwood number Rayleigh–Taylor flow are derived in Appendix C.

II. DESCRIPTION OF THE DIRECT NUMERICAL SIMULATION DATASET

The DNS dataset and its validation are summarized here. The statistical averages used to define mean and fluctuating fields, correlations of fluctuating fields, and the transport equation budgets are also presented.

A. Summary of the simulation and its validation

1. *Initial conditions and equations solved*

The DNS was modeled after a hot/cold water Rayleigh–Taylor mixing experiment.[6] The initial conditions were taken from initial perturbations in the x- and y-directions (perpendicular to gravity) in the experiment. Density perturbations in the streamwise x-direction were measured using a thermocouple placed on the center plane $z = 0$ a short distance downstream from the trailing edge of the splitter plate. Temperature measurements were converted to density using the equation of state of water. Interfacial perturbations were also measured in the spanwise y-direction using planar laser-induced fluorescence. Spectra of the perturbations were then used to formulate the initial interfacial perturbation in the DNS. Velocity fluctuations at the onset of the instability were measured using particle-image velocimetry. An initial velocity field based on the measured center plane initial vertical velocity variance spectrum was then constructed (no assumption of isotropy was made).

The variable-density incompressible density, momentum, and heavy-fluid mass fraction equations

$$\frac{\partial \rho}{\partial t} + \frac{\partial}{\partial x_j}(\rho\, u_j) = 0\,, \tag{1a}$$

$$\frac{\partial}{\partial t}(\rho\, u_i) + \frac{\partial}{\partial x_j}(\rho\, u_i\, u_j) = \rho\, g_i - \frac{\partial p}{\partial x_i} + \frac{\partial \sigma_{ij}}{\partial x_j}\,, \tag{1b}$$

$$\frac{\partial}{\partial t}(\rho\, m_1) + \frac{\partial}{\partial x_j}(\rho\, m_1\, u_j) = \frac{\partial}{\partial x_j}\left(\rho\, D\, \frac{\partial m_1}{\partial x_j}\right) \tag{1c}$$

were solved using a spectral/compact difference scheme,[12] where ρ is the density, u_i is the velocity, $g_i = (0,0,-g)$ is gravity, p is the pressure, $\sigma_{ij} = \mu\left(\partial u_i/\partial x_j + \partial u_j/\partial x_i - \frac{2}{3}\delta_{ij}\partial u_k/\partial x_k\right)$ is the viscous stress tensor with dynamic viscosity $\mu = \rho\nu$

and kinematic viscosity $\nu = (\mu_1 + \mu_2)/(\rho_1 + \rho_2)$, and D is the mass diffusivity. The Atwood and Schmidt numbers are $A = (\rho_1 - \rho_2)/(\rho_1 + \rho_2) = 7.5 \times 10^{-4}$ and $\mathrm{Sc} = \nu/D = 7$. The densities, dynamic viscosities, and other quantities are summarized in Table II of Ref. 1.

2. *Validation of DNS by comparison to experimental data*

The DNS was validated by comparing large-scale, turbulence, and mixing statistics with measurements from the water channel experiment.[1] The simulated temporally developing mixing layer was related to the downstream spatially developing flow in the experiment using the Taylor hypothesis $x = \overline{u}_x t$, where $\overline{u}_x$ is the mean velocity of each water stream entering the channel (there is no imposed shear). This can be interpreted as transforming the DNS to a reference frame moving with the mean velocity of the streams in the streamwise direction. The validity of the Taylor hypothesis was verified *a posteriori* by noting that the temporal features in the experimental data are correctly captured in the simulation.

Integral scale quantities were compared, including the bubble front mixing layer width h_b and self-similar growth parameter α_b. The DNS was in good agreement with the experimental late-time self-similar growth of the bubble front $h_b(t) = \alpha_b A g t^2$ with $\alpha_b \approx 0.07$. Turbulence statistics from the DNS were also compared to available experimental data. The center plane velocity variances were all in good agreement at early times, but the simulation underestimated the variances from the experiment at later times. Vertical velocity and density variance spectra were in very good agreement between the DNS and experiment at all times. The evolution of the molecular mixing parameter on the center plane θ was also in good agreement with the experiment; while θ from the DNS was lower than measured after the transition to a more turbulent three-dimensional state, the uncertainties in the measurements from both overlapped. At intermediate times, θ from the DNS was $\approx 20\%$ lower than in the experiment. However, at the latest time in the experiment, $\theta \approx 0.6$ compared to $\theta \approx 0.55$ from the DNS.

B. Computation of mean and fluctuating fields

The statistical analysis of turbulent mixing layers requires averaging over an ensemble of realizations. Due to the extreme computational requirements of DNS of Rayleigh–Taylor unstable flow, it is not feasible to perform an ensemble of high-resolution simulations for averaging purposes. Hence, invoking the ergodic hypothesis, an ensemble average of a field $\phi(\mathbf{x},t)$ is defined as the Reynolds average over the statistically homogeneous plane[12,13]

$$\overline{\phi}(z,t) = \frac{1}{L_x\, L_y} \int_0^{L_x} \int_0^{L_y} \phi(\mathbf{x},t)\, dy\, dx\,, \tag{2}$$

such that ϕ can be decomposed into mean and fluctuating components $\phi(\mathbf{x},t) = \overline{\phi}(z,t) + \phi(\mathbf{x},t)'$. The fluctuation of the field (denoted by a prime) averages to zero in a given plane, $\overline{\phi'} = 0$. To facilitate the analysis of variable-density effects,[14] a Favre average

$$\widetilde{\phi}(z,t) = \frac{\overline{\rho\,\phi}(z,t)}{\overline{\rho}(z,t)} = \frac{\int_0^{L_x}\int_0^{L_y} \rho(\mathbf{x},t)\,\phi(\mathbf{x},t)\,dy\,dx}{\int_0^{L_x}\int_0^{L_y} \rho(\mathbf{x},t)\,dy\,dx} \tag{3}$$

is also considered, such that $\phi(\mathbf{x},t) = \widetilde{\phi}(z,t) + \phi(\mathbf{x},t)''$. A Favre fluctuating field does not average to zero, i.e., $\overline{\phi''} \neq 0$; however, $\overline{\rho\phi''} = 0$. Averaging over xy-planes results in each mean field or correlation becoming only a function of the vertical coordinate z, so that the transport equations are reduced to statistically one-dimensional equations across the vertical width of the expanding mixing layer. As buoyancy-driven turbulence does not generally satisfy the Boussinesq approximation,[15] Favre averages are typically used: while this approximation is valid for the flow considered here, the Favre-averaged framework is retained for generality.

C. Computation of mean field gradients

Gradients were calculated using spectral methods in the x- and y-directions and sixth-order finite differencing in the z-direction. Profiles of averaged quantities are not always statistically converged and may be oscillatory at later times when the mixing layer becomes large and fewer structures are present. In order to preserve the trends of the gradients, the profiles are smoothed before their gradient is calculated by a locally-weighted scatterplot smoothing (LOWESS) technique.[16] In contrast to a moving average that averages all of the data points in a given window, the LOWESS method calculates a smoothed value by computing a weighted linear least-squares regression over the window. This does not change the smooth profiles at the two earliest times, and reduces oscillations at later times.

III. MEAN FLOW STRUCTURE

Budgets of the momentum and heavy-fluid mass fraction equations describing the large-scale growth of the mixing layer are presented here at several times. Four times representative of the linear, weakly-nonlinear, strongly-nonlinear, and weakly-turbulent regimes were chosen, and their corresponding Reynolds numbers are given in Table I. For all of the mean and turbulence budgets presented, quantities will be nondimensionalized using density, length, and time scales corresponding to linear instability theory:[13,17]

$$\rho_c = \frac{\rho_1 + \rho_2}{2}\ ,\ \ell_c = \left(\frac{\nu^2}{g\,A}\right)^{1/3}\ ,\ t_c = \left(\frac{\nu}{g^2 A^2}\right)^{1/3}\ , \tag{4}$$

t	t/t_c	τ	Re_h	$\mathrm{Re}_h^{\dot{h}}$	Re_λ^w
1.36	5.13	0.21	21	47	7.3
3.32	12.6	0.50	137	352	22.5
6.65	25.1	1.01	708	1620	51.1
10.03	37.9	1.52	1712	2666	90.4

TABLE I: Dimensional and dimensionless profile times, t (in units of s) and t/t_c, respectively, and the corresponding integral scale Reynolds numbers, $\mathrm{Re}_h(t) = 0.35\sqrt{gAh^3}/\nu$ and $\mathrm{Re}_h^{\dot{h}}(t) = (h\mathrm{d}h/\mathrm{d}t)/\nu$, and Taylor scale Reynolds number $\mathrm{Re}_\lambda^w(z,t) = \lambda_T^w\sqrt{\overline{w'^2}}/\nu$. The integral scale Reynolds numbers are based on 5%–95% mixing layer width profiles.[1,11] For reference, the corresponding time normalized by the Boussinesq scaling $\tau = t\sqrt{gA/H}$ (where A is the Atwood number, g is Earth's gravity, and $H = 32$ cm is the height of the water channel in the experiment) is also given.

which are $\rho_c = 0.998$ g/cm^3, $\ell_c = 0.051$ cm, and $t_c = 0.264$ s for the flow considered here with $g = 981$ cm/s^2, $\nu = 0.01$ cm^2/s and $A = 7.5\times10^{-4}$. The velocity scale is $u_c = \ell_c/t_c = 0.193$ cm/s. Profiles are plotted along the z-axis normalized by the instantaneous mixing layer width $h(t)$ based on the 5%–95% volume fraction profile thresholds,[1] so that the vertical extent of the layer is $z/h(t) \in [-1/2, 1/2]$ with the heavy-fluid side $z/h(t) > 0$ and the light-fluid side $z/h(t) < 0$.

A. Mean momentum transport

The Reynolds-averaged Navier–Stokes equation is

$$\overline{\rho}\left(\frac{\partial}{\partial t} + \widetilde{u}_j\,\frac{\partial}{\partial x_j}\right)\widetilde{u}_i = \overline{\rho}\,g_i - \frac{\partial\overline{p}}{\partial x_i} + \frac{\partial\overline{\sigma}_{ij}}{\partial x_j} - \frac{\partial\tau_{ij}}{\partial x_j}\,, \quad (5)$$

where the averaged viscous stress tensor is $\overline{\sigma}_{ij} = \overline{\mu}\left(\partial\widetilde{u}_i/\partial x_j + \partial\widetilde{u}_j/\partial x_i - \frac{2}{3}\delta_{ij}\partial\widetilde{u}_k/\partial x_k\right)$ and the unclosed Reynolds stress tensor is $\tau_{ij} = \overline{\rho}\,\widetilde{u_i''u_j''}$.[18,19] As viscosity varies only slightly between the fluid components (so that $\overline{\mu'\phi'} \ll \overline{\mu}\,\overline{\phi}$), all higher order terms in $\overline{\sigma}_{ij}$ involving μ' can be neglected.[18] Equation (5) reduces to

$$\overline{\rho}\left(\frac{\partial}{\partial t} + \widetilde{w}\,\frac{\partial}{\partial z}\right)\widetilde{w} = -\overline{\rho}\,g - \frac{\partial\overline{p}}{\partial z} + \frac{\partial\overline{\sigma}_{33}}{\partial z} - \frac{\partial\tau_{33}}{\partial z}\,. \quad (6)$$

Figure 1 shows the mean vertical velocity and mean density gradient. The mean vertical velocity, which is negative as a result of the relationship $\widetilde{w} = \overline{w} + \overline{\rho'w'}/\overline{\rho} = \overline{w} - \overline{w''}$, where $\overline{\rho'w'}$ is the turbulent density flux of the heavy fluid in the downward direction. The relation between the Favre and Reynolds averaged vertical velocity is obtained by averaging $\rho'w' = (\rho-\overline{\rho})(w-\overline{w})$, which gives $\overline{\rho'w'} = \overline{\rho w} - \overline{\rho}\,\overline{w} = \overline{\rho}\widetilde{w} - \overline{\rho}\,\overline{w}$. The Favre-averaged divergence $\partial\widetilde{u}_i/\partial x_i \to \partial\widetilde{w}/\partial z$ remains small,[7] decreases in time, and rapidly decreases after the transition to a weakly-turbulent state after $t/t_c \approx 12.6$. The mean velocities in the homogeneous directions $\widetilde{u}$ and $\widetilde{v}$ are small

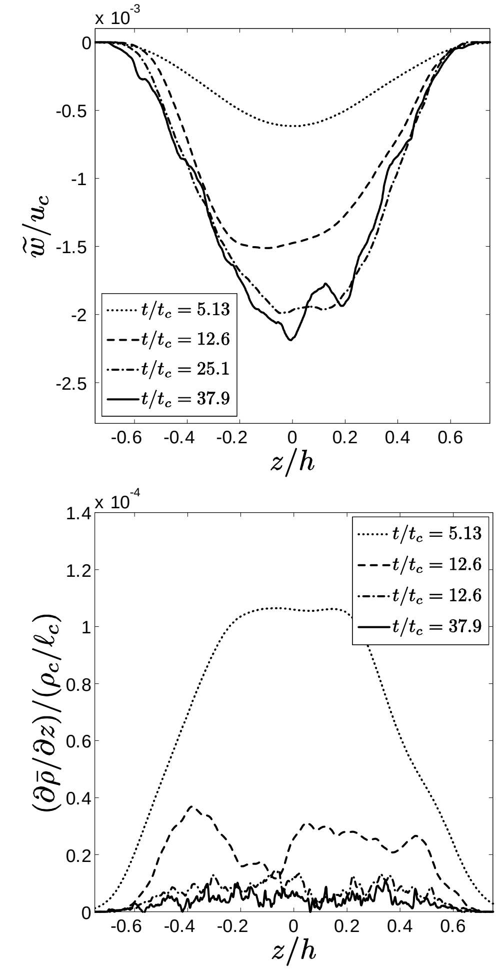

FIG. 1: Profiles of the mean vertical velocity $\widetilde{w}$ normalized by u_c (top) and mean density gradient normalized by ρ_c/ℓ_c (bottom) at various dimensionless times.

(not shown). The mean density profiles (not shown) collapse like the $\widetilde{m}_1$ profiles shown in Fig. 3, and indicate that the 5 $^\circ$K temperature difference between the water streams results in a very small difference in their densities. The mean density gradient $\partial\overline{\rho}/\partial z \approx (\rho_1-\rho_2)/h(t)$ decreases as the mixing layer grows with increasing h. At the latest time, the gradient has decreased from its early time value by ≈ 20, and is much flatter (consistent with a linear $\overline{\rho}$ profile). Using $\Delta\rho = \rho_1-\rho_2 \sim 1.55\times10^{-3}$ g/cm^3 and $h \sim 15$ cm at the latest time gives $(\partial\overline{\rho}/\partial z)/(\rho_c/\ell_c) \sim (\Delta\rho/h)/(\rho_c/\ell_c) \sim 5.1\times10^{-6}$, in good agreement with the profile in Fig. 1. The mean pressure $\overline{p}$ (not shown) is linear across the layer, becoming progressively steeper as the flow evolves, and its gradient approximately collapses. The flow attains a nearly hydrostatic equilibrium $\partial\overline{p}/\partial z \sim -\rho_0 g$ by $t/t_c \approx 12.6$.

The budget of the mean vertical momentum equation (6) is shown in Fig. 2, where the total forcing, diffusive, and Reynolds stress terms are $F^{\widetilde{w}} = -\overline{\rho}g - \partial\overline{p}/\partial z$, $D^{\widetilde{w}} = \partial\overline{\sigma}_{33}/\partial z$, $R^{\widetilde{w}} = -\partial\tau_{33}/\partial z$, respectively. All terms have their largest magnitude at $t/t_c = 5.13$. Advection

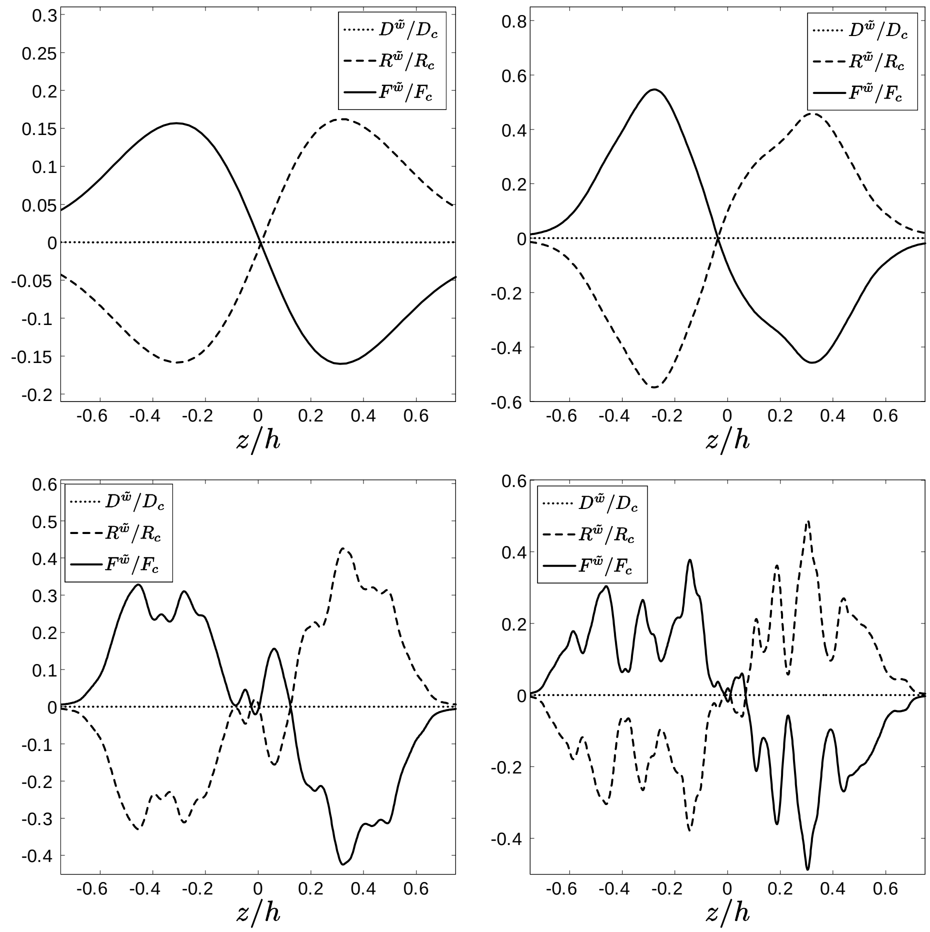

FIG. 2: Profiles of the dominant terms in the mean vertical momentum equation (6) normalized by $D_c = R_c = F_c = \rho_c u_c/t_c$ at $t/t_c = 5.13$ (top left), 12.6 (top right), 25.1 (bottom left), and 37.9 (bottom right).

$A^{\widetilde{w}} = \overline{\rho}\widetilde{w}\partial\widetilde{w}/\partial z$ is negligible in small Atwood number flows as a consequence of nearly zero mean velocity and velocity gradients and is not shown. The diffusive term smooths fluctuations and gradients in $\widetilde{w}$, and increases with time. The contribution of $D^{\widetilde{w}}$ also remains negligible, with both $A^{\widetilde{w}}$ and $D^{\widetilde{w}}$ approximately averaging to zero.

The total forcing and Reynolds stress gradient almost balance one another such that $F^{\widetilde{w}} \approx -R^{\widetilde{w}}$ at each time, indicating that *the Reynolds stress contribution cannot be neglected*, even at small Atwood numbers. The slight imbalance leads to the growth of $\widetilde{w}$. Both $F^{\widetilde{w}}$ and $R^{\widetilde{w}}$ are nearly symmetric about the center plane, with an asymmetry slowly growing in time. The total forcing is positive on the light-fluid side $z/h < 0$ and negative on the heavy-fluid side $z/h > 0$, and vice versa for the Reynolds stress term. The profiles extend far beyond the mixing layer edges $z/h = \pm 0.5$ at the earliest time. The near stationarity of $\widetilde{w}$ between $t/t_c = 25.1$ and 37.9 results from $F^{\widetilde{w}} \approx -R^{\widetilde{w}}$, i.e., $\partial\widetilde{w}/\partial t \approx 0$ at late times. The order of magnitude in Eq. (B1) shows that the viscous term is proportional to $\widetilde{u}$, and is thus, negligible in the energy balance. The spatial integral of Eq. (B1) is $\frac{d}{dt}[\overline{\rho}\widetilde{w}(t)] = F(t) - D(t) - R(t) \approx F(t) - R(t)$, representing a balance between stationary terms both of $\mathcal{O}(\rho_0 g)$: $|F(t)| = |-\overline{\rho}g - \partial p/\partial z|$.

B. Mean heavy-fluid mass fraction transport

The heavy-fluid mass fraction is $m_1 = f_1\rho_1/\rho$, with volume fraction $f_1 = (\rho - \rho_2)/(\rho_1 - \rho_2)$, so that $\widetilde{m}_1 = \overline{f_1\rho_1}/\overline{\rho}$. The mean light-fluid mass fraction is $\widetilde{m}_2 = 1 - \widetilde{m}_1$. The Reynolds-averaged heavy-fluid mass fraction equation is

$$\overline{\rho}\left(\frac{\partial}{\partial t} + \widetilde{u}_j\,\frac{\partial}{\partial x_j}\right)\widetilde{m}_1 = T^{\widetilde{m}_1}\,, \tag{7}$$

where the total (turbulent plus molecular) transport term is ($\mathrm{Sc} = \overline{\nu}/\overline{D} = 7$ is the Schmidt number)

$$\begin{aligned} T^{\widetilde{m}_1} &= -\frac{\partial}{\partial x_j}\left(\overline{\rho}\,\widetilde{m_1'' u_j''} - \frac{\overline{\mu}}{\mathrm{Sc}}\,\frac{\partial\widetilde{m}_1}{\partial x_j}\right) \\ &\to -\frac{\partial}{\partial z}\left(\overline{\rho}\,\widetilde{m_1'' w''} - \frac{\overline{\mu}}{\mathrm{Sc}}\,\frac{\partial\widetilde{m}_1}{\partial z}\right). \end{aligned} \tag{8}$$

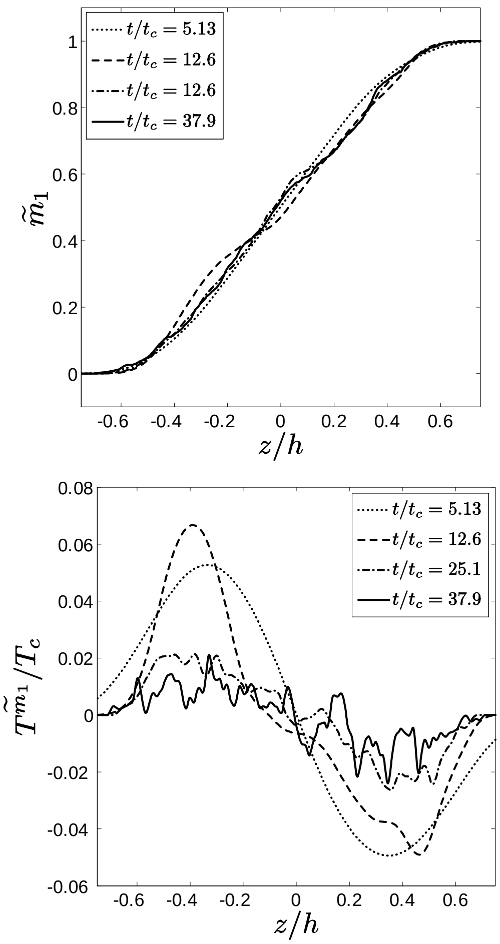

FIG. 3: Profiles of the mean heavy-fluid mass fraction $\widetilde{m}_1$ (top) and of the mean heavy-fluid mass fraction transport $T^{\widetilde{m}_1}$ (8) normalized by $T_c = \rho_c/t_c$ (bottom) at various dimensionless times.

The mean heavy-fluid mass fraction is bounded, $0 \leq \widetilde{m}_1 \leq 1$, and in the absence of chemical reactions, has no source or sink terms: molecular and turbulent diffusion are the only mechanisms for the transport of $\widetilde{m}_1$.

The mean heavy-fluid mass fraction profiles shown in Fig. 3 collapse to an approximately linear form over $z/h(t) \in [-0.3, 0.3]$, similar to the volume fraction profiles in water channel experiments.[8] This is expected as the mean mass and volume fraction are linearly related. Thus, diffusive transport of $\widetilde{m}_1$ is only significant at very early times when the mixing layer width h and the Reynolds number are small, resulting in large mean gradient $\partial\widetilde{m}_1/\partial z$ and small flux $\widetilde{m_1'' w''}$.

The mean advection $\overline{\rho}\widetilde{w}\partial\widetilde{m}_1/\partial z$ is very small and is not shown. The transport $T^{\widetilde{m}_1}$ shown in Fig. 3 is positive for $z/h < 0$, indicating accumulation of heavy fluid, and negative for $z/h > 0$, indicating loss of heavy fluid as the heavy fluid continues to fall into the lighter fluid. The magnitude of $T^{\widetilde{m}_1}$ decreases rapidly between $t/t_c = 12.6$ and 25.1, and then changes relatively little up to $t/t_c = 37.9$. The contributions to $T^{\widetilde{m}_1}$ can be decomposed into turbulent and diffusive fluxes $F_t^{\widetilde{m}_1} = \overline{\rho}\widetilde{m_1'' w''}$ and $F_d^{\widetilde{m}_1} = -(\overline{\mu}/\mathrm{Sc})\,\partial\widetilde{m}_1/\partial z$, respectively. The turbulent flux is negative, as the net vertical velocity fluctuations are directed downward. The diffusive flux is always negligible.[7] The spatial integral of Eq. (B2) is $\frac{d}{dt}[\overline{\rho}\widetilde{m}_1(t)] = 0$, indicating conservation of mass fraction. At late-time, $T^{\widetilde{m}_1}/T_c \sim (\rho_0 m_{rms} u_h/h)/T_c \sim 0.002$, in reasonable agreement with the profile shown in Fig. 3.

IV. MECHANICAL TURBULENT FLOW STRUCTURE

The flow dynamics are governed by the competition of production, dissipation, and transport mechanisms. Production terms arising from buoyancy, shear, and pure turbulence effects are positive-definite over the mixing layer. Dissipation terms arising from turbulence destruction mechanisms remove turbulent kinetic energy and scalar variance from the flow. Finally, transport terms redistribute the turbulent fields conservatively within the layer and do not contribute to the global energy balance.

The budgets of the mechanical turbulent transport equations are computed from the DNS data and discussed here. In addition to the statistics previously considered at the center plane of the mixing layer,[1,11] statistics across the mixing layer are presented here. Of principal importance to transport in Rayleigh–Taylor flow is the evolution and spatial distribution of the turbulent kinetic energy and its dissipation rate.

A. Turbulent kinetic energy transport

1. *Reynolds stress components and turbulent kinetic energy*

While mean velocity gradients are of minimal importance to the dynamics at small Atwood number, the turbulent force $\partial\tau_{ij}/\partial x_j$ in Eq. (5) represents the mean transport of fluctuating momentum by turbulent velocity fluctuations, and energy exchange between the turbulence and mean flow. The components of $\tau_{ij}/\overline{\rho}$ shown in Fig. 4 all grow with time. The vertical velocity variance $\widetilde{w''^2}$ is largest, indicating that transport of $\widetilde{w''^2}$ provides the most important energy redistribution mechanism. The off-diagonal shear stresses are positive and negative over the layer and are much smaller than the diagonal components.[7] Comparing $\widetilde{u''^2}$ and $\widetilde{v''^2}$ shows that anisotropy in the x- and y-directions persists to late times for this flow.

The turbulent kinetic energy per unit mass $\widetilde{E''} = \widetilde{u_i''^2}/2$ shown in Fig. 5 is peaked in the mixing layer core and grows as velocity fluctuations increase; $\widetilde{E''}$ is broadly distributed over the narrow mixing layer at the earliest times, becoming narrower at the latest time when the turbulence is most intense within the core. The Reynolds-

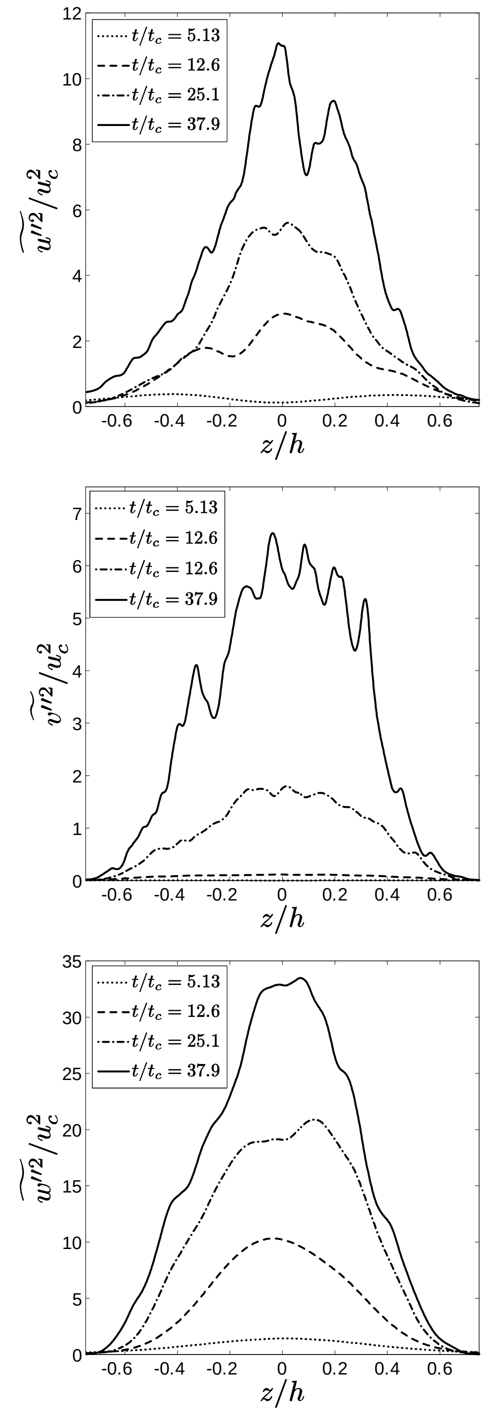

FIG. 4: Profiles of the diagonal components of the Reynolds stress tensor $\widetilde{u_i''^2}$ normalized by u_c^2 at various dimensionless times.

averaged turbulent kinetic energy per unit mass $\overline{E'} = \overline{u_i'^2}/2$ is virtually identical to $\widetilde{E''}$ and is not shown. At late-time, $\widetilde{E''}/u_c^2 \sim u_h^2/\left(2u_c^2\right) \sim 43$, in agreement with the order of magnitude of the profile in Fig. 5.

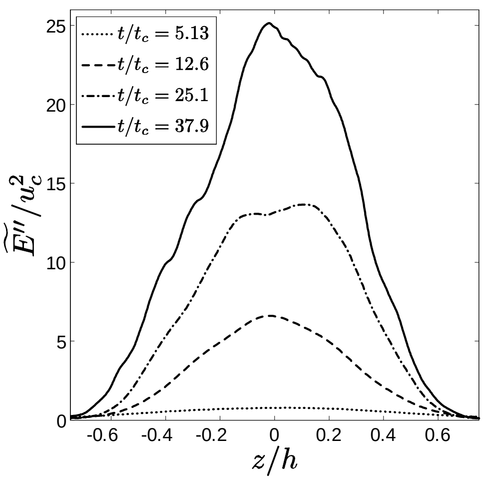

FIG. 5: Profiles of the turbulent kinetic energy per unit mass $\widetilde{E''}$ normalized by u_c^2 at various dimensionless times.

2. Potential energy, kinetic energy, and dissipation dynamics

Energy is removed from the mean kinetic energy ($\widetilde{E} = \widetilde{u}_i^2/2$) by shearing forces, transferred to the turbulent kinetic energy, and converted to thermal energy by viscous dissipation in classical shear-driven turbulent boundary layers, shear layers, wakes, and jets. However, in Rayleigh–Taylor instability-driven mixing, the turbulent kinetic energy is driven by release of gravitational potential energy by the heavy fluid falling into the light fluid.

The total mean potential energy per unit volume is

$$\overline{U}(t) = -\frac{1}{L_z}\int_{-L_z/2}^{L_z/2} \overline{\rho}\, g_z\, z\, dz = \frac{g}{L_z}\int_{-L_z/2}^{L_z/2} \overline{\rho}\, z\, dz \qquad (9)$$

and the cumulative potential energy released is $\Delta\overline{U}(t) = \overline{U}(0) - \overline{U}(t)$, both of which are shown in Fig. 6. The total mean kinetic energy per unit volume

$$\widetilde{E}(t) = \frac{1}{L_z}\int_{-L_z/2}^{L_z/2} \widetilde{E}(z,t)\, dz\,, \qquad (10)$$

total turbulent kinetic energy per unit volume

$$\widetilde{E''}(t) = \frac{1}{L_z}\int_{-L_z/2}^{L_z/2} \widetilde{E''}(z,t)\, dz\,, \qquad (11)$$

and cumulative turbulent kinetic energy dissipated per unit volume

$$D^{\widetilde{E''}}(t) = \frac{1}{L_z}\int_0^t \int_{-L_z/2}^{L_z/2} \widetilde{\epsilon''}(z,t')\, dz\, dt'\,, \qquad (12)$$

are also shown in Fig, 6 [see Eq. (15d) for the definition of the turbulent kinetic energy dissipation rate per unit mass $\widetilde{\epsilon''}$], where the conversion of potential energy to

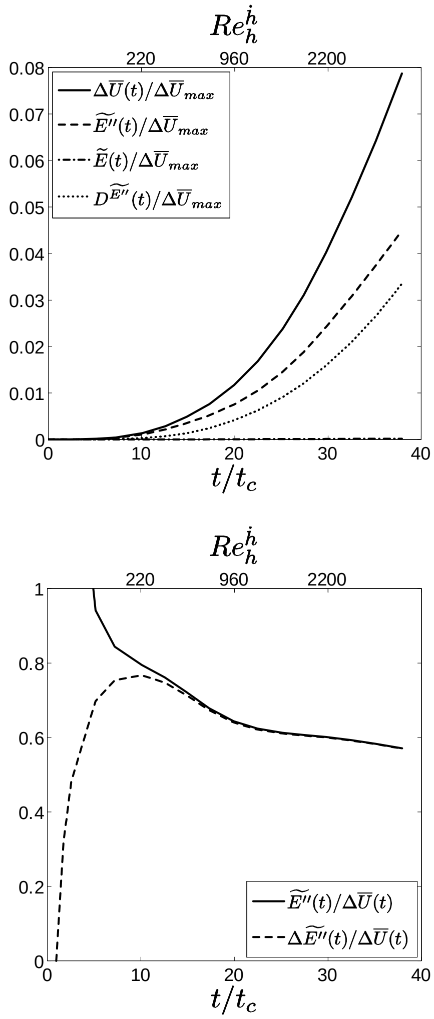

FIG. 6: Evolution of potential energy released $\Delta\overline{U}(t)$, turbulent kinetic energy $\widetilde{E''}(t)$, mean kinetic energy $\widetilde{E}(t)$, and cumulative turbulent kinetic energy dissipated $D^{\widetilde{E''}}(t)$, all normalized by the maximum amount of potential energy that can be released $\Delta U_{max} = U(0) - (g/L_z)\int_{-L_z/2}^{0} \rho_2 z dz + (g/L_z)\int_0^{L_z/2} \rho_1 z dz$ (top). Evolution of the ratio of turbulent kinetic energy to potential energy released (bottom).

turbulent kinetic energy is evident. The cumulative turbulent kinetic energy gained is $\Delta\widetilde{E''}(t) = \widetilde{E''}(t) - \widetilde{E''}(0)$. The conversion of potential energy to kinetic energy is slowed as molecular mixing progresses. The ratio of turbulent kinetic energy to potential energy released is also shown in Fig. 6, where $\widetilde{E''}(t)/\Delta\overline{U}(t) \approx 0.57$ at the latest time—somewhat larger than $\widetilde{E''}(t)/\Delta\overline{U}(t) \approx 0.48$–0.52 inferred from water channel[5] and gas channel,[9] measurements and from other MILES and DNS.[20–22] However, $\widetilde{E''}(t)/\Delta\overline{U}(t)$ in the current DNS is still decreasing at $t/t_c = 37.9$. The initial conditions used in a simulation can affect this ratio,[21] where a wide range $\widetilde{E''}(t)/\Delta\overline{U}(t) \approx 0.48$–0.70 was reported. The Froude number $Fr_h = u_h/\sqrt{gh} \sim 0.015$ is related to the ratio of the turbulent kinetic energy gained $\rho_0 \Delta\widetilde{E''} \approx \rho_0 u_h^2$ to the mean potential energy released $\Delta\overline{U} \sim \rho_{rms} g h/\rho_0$ by $\Delta\widetilde{E''}/\Delta\overline{U} \sim (\rho_0/\rho_{rms})\, Fr_h^2 \approx 0.65$ at the latest time ($\sim 14\%$ larger than the ratio from the DNS). The ratio of mean-to-turbulent kinetic energy always remains less than 0.01. The mean kinetic energy transport equation approximately reduces to

$$\overline{\rho}\, g\, \widetilde{w} + \widetilde{w}\, \frac{\partial \overline{p}}{\partial z} + \widetilde{w}\, \frac{\partial \tau_{33}}{\partial z} = 0\,. \tag{13}$$

3. Turbulent production, dissipation, and transport

The turbulent kinetic energy transport equation is

$$\begin{aligned} \overline{\rho}\left(\frac{\partial}{\partial t} + \widetilde{u}_j\, \frac{\partial}{\partial x_j}\right)\widetilde{E''} \;&=\; P_b^{\widetilde{E''}} + P_s^{\widetilde{E''}} + \Pi^{\widetilde{E''}} \\ &\quad -D^{\widetilde{E''}} + T^{\widetilde{E''}}\,, \end{aligned} \tag{14}$$

where the buoyancy production, shear production, pressure–dilatation, turbulent dissipation, and transport are

$$P_b^{\widetilde{E''}} = -\overline{u_j''}\, \frac{\partial \overline{p}}{\partial x_j} \to -\overline{w''}\, \frac{\partial \overline{p}}{\partial z}\,, \tag{15a}$$

$$P_s^{\widetilde{E''}} = -\overline{\rho}\, \widetilde{u_i''\, u_j''}\, \frac{\partial \widetilde{u}_i}{\partial x_j} \to -\overline{\rho}\, \widetilde{u_i''\, w''}\, \frac{\partial \widetilde{u}_i}{\partial z}\,, \tag{15b}$$

$$\Pi^{\widetilde{E''}} = \overline{p'\, \frac{\partial u_k''}{\partial x_k}}\,, \tag{15c}$$

$$D^{\widetilde{E''}} = \overline{\rho}\, \widetilde{\epsilon''} = \overline{\sigma_{ij}\, \frac{\partial u_i''}{\partial x_j}}\,, \tag{15d}$$

$$\begin{aligned} T^{\widetilde{E''}} \;&=\; -\frac{\partial}{\partial x_j}\left(\overline{\rho}\, \widetilde{E''\, u_j''} + \overline{p'\, u_j''} - \overline{\sigma_{ij}\, u_i''}\right) \\ &\to\; -\frac{\partial}{\partial z}\left(\overline{\rho}\, \widetilde{E''\, w''} + \overline{p'\, w''} - \overline{\sigma_{i3}\, u_i''}\right), \end{aligned} \tag{15e}$$

respectively.[18,19] The qualitative structure of the dominant terms in the $\widetilde{E''}$ transport equation shown in Fig. 7 remains similar for all times. Buoyancy production generates turbulent kinetic energy within the mixing layer $|z/h| < 0.5$, while turbulent dissipation $D^{\widetilde{E''}}$ removes turbulent kinetic energy from the layer. The profiles of $P_b^{\widetilde{E''}}$ exhibit some asymmetry within the core for $t/t_c \geq 12.6$, and are very similar at $t/t_c = 25.1$ and 37.9.

The mean advection $\overline{\rho}\widetilde{w}\partial\widetilde{E''}/\partial z$ is very small and is not shown. As the mean velocity gradient contribution to the turbulent kinetic energy production is negligible, the magnitude of $P_s^{\widetilde{E''}}$ is considerably smaller than $P_b^{\widetilde{E''}}$. There is no discernible structure in the profiles of

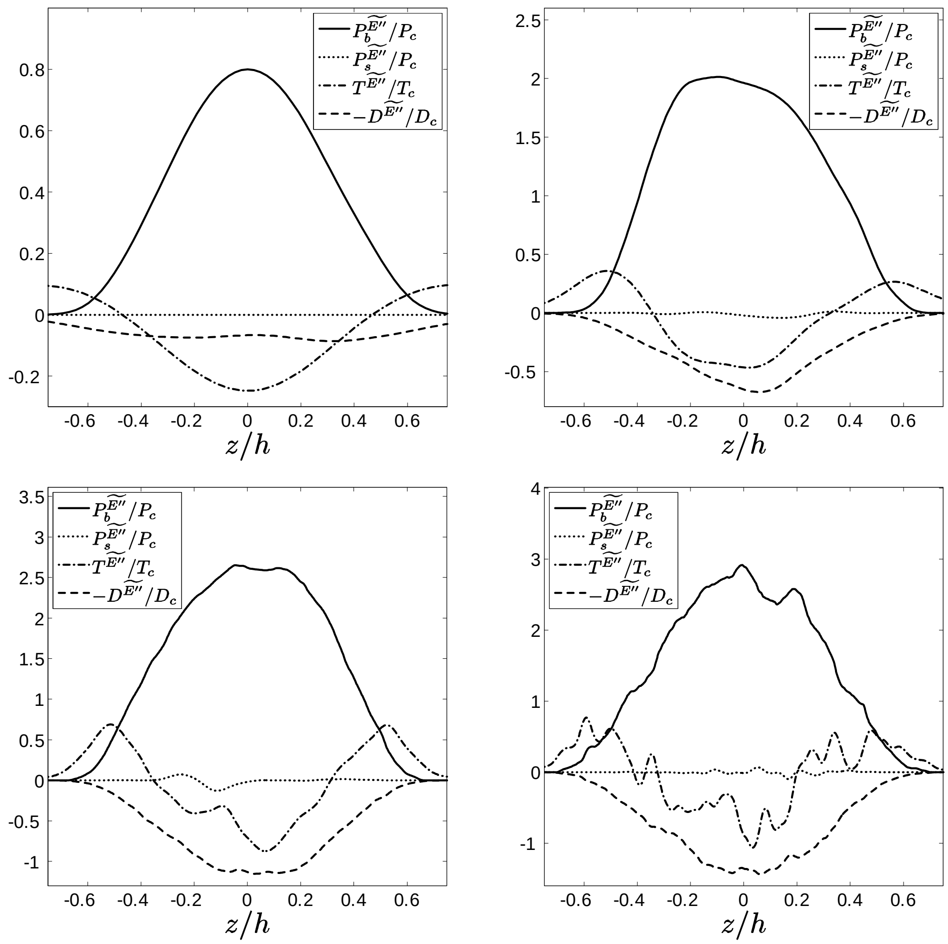

FIG. 7: Profiles of the dominant terms in the turbulent kinetic energy transport equation (14) normalized by $P_c = T_c = D_c = \rho_c u_c^2/t_c$ at $t/t_c = 5.13$ (top left), 12.6 (top right), 25.1 (bottom left), and 37.9 (bottom right).

$P_s^{\widetilde{E''}}$, which have positive and negative values and approximately average to zero.[7] The buoyancy production broadens rapidly between $t/t_c = 5.13$ and 12.6, and is large in the mixing layer core $z/h \in [-0.3, 0.3]$. The profiles do not change significantly between $t/t_c = 25.1$ and 37.9. On average, the pressure–dilatation correlation $\Pi^{\widetilde{E''}}$ (not shown) is $\Pi^{\widetilde{E''}} < 0$ for $z/h < 0$ and $\Pi^{\widetilde{E''}} > 0$ for $z/h > 0$; $\Pi^{\widetilde{E''}}$ remains negligible for the small Atwood number flow here.[7] The flow here is incompressible, but $\Pi^{\widetilde{E''}} \neq 0$ as a result of the miscibility of the fluids. For miscible mixtures,[23] $\nabla \cdot \mathbf{u} = -\nabla \cdot (D\, \boldsymbol{\nabla} \ln \rho) \neq 0\,$, scales with the local density gradient.

Similar to buoyancy production, turbulent dissipation is also approximately Gaussian with peaks near $z/h \approx 0$. In Rayleigh–Taylor mixing, the turbulent kinetic energy grows due to the continual release of potential energy, so that production of $\widetilde{E''}$ does not equal its dissipation. Conservative redistribution of $\widetilde{E''}$ throughout the layer is given by the transport $T^{\widetilde{E''}}$. Regions with $T^{\widetilde{E''}} > 0$ gain turbulent kinetic energy, and regions with $T^{\widetilde{E''}} < 0$ lose turbulent kinetic energy; $\widetilde{E''}$ is transported from the central core, $|z/h| \lesssim 0.3$, to the edges of the layer, i.e., down-gradient from regions of high energy to lower energy. The initial profile is small in magnitude, growing rapidly as velocity fluctuations increase. The profiles of $T^{\widetilde{E''}}$ at $t/t_c = 25.1$ and 37.9 are similar on average. The profiles approach zero near $z/h \approx \pm 0.7$, and not at the edges of the mixing layer $z/h = \pm 0.5$. The Fourier space dynamics of turbulent kinetic energy transfer in Rayleigh–Taylor flow was previously considered using data from a $512^2 \times 2040$ DNS.[24]

Referring to the order of magnitude in Eq. (B3), the viscous contribution diminishes as the flow evolves to larger Reynolds numbers. Buoyancy production, turbulent dissipation, and transport can be estimated at late times as $P_b^{\widetilde{E''}}/P_c \sim \rho_{rms} g u_h/P_c \sim 4.3$, $D^{\widetilde{E''}}/D_c \sim (\rho_0 u_h^3/h)/D_c \sim 2.8$, and $T^{\widetilde{E''}}/T_c \sim \rho_0 u_h^3/(2hT_c) \sim 1.4$, consistent with the order of magnitude of the maxima and minima of the profiles in Fig. 7.

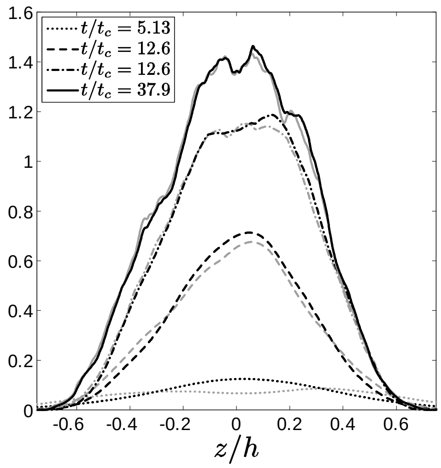

FIG. 8: Profiles of the turbulent kinetic energy dissipation rates $\overline{\epsilon'}$ (black) and $\widetilde{\epsilon''}$ (grey) normalized by u_c^2/t_c at various dimensionless times.

B. Turbulent kinetic energy dissipation rate transport

1. The turbulent kinetic energy dissipation rate

The transport equation for the incompressible turbulent kinetic energy (pseudo) dissipation rate

$$\overline{\epsilon'} = \overline{\nu}\,\overline{\left(\frac{\partial u_i'}{\partial x_j}\right)^2} \tag{16}$$

is examined here. The difference between $\overline{\epsilon'}$ and the true kinetic energy dissipation rate density per unit mass $\epsilon = 2\overline{\nu}\,\overline{S_{ij}' S_{ij}'}$, where $S_{ij}' = \frac{1}{2}\left(\partial u_i'/\partial x_j + \partial u_j'/\partial x_i\right)$ is the fluctuating strain-rate tensor, is $\epsilon - \overline{\epsilon'} = \overline{\nu}\partial^2\tau_{ij}/\partial x_i \partial x_j$, which is generally small and typically neglected.[25] This was also found to be true for the present flow.

The incompressible (16) and general dissipation rate per unit mass $\widetilde{\epsilon''} = \overline{\nu}\overline{(\partial u''/\partial x_j)^2}$ shown in Fig. 8 are very similar, as expected for small Atwood number mixing layers. Like $\widetilde{E''}$ shown in Fig. 5, $\overline{\epsilon'}$ is peaked in the mixing layer core and grows as vortex stretching increases with Reynolds number; $\overline{\epsilon'}$ is broadly distributed over the narrow mixing layer at the earliest times, becoming narrower at the latest time. At late-time, $\overline{\epsilon'}/\left(u_c^2/t_c\right) \sim u_h^3 t_c/\left(2hu_c^2\right) \sim 1.4$, in very good agreement with the profile in Fig. 8.

2. Turbulent production, destruction, and transport

The transport equation for $\overline{\epsilon'}$,[25–29] generalized here to include a production term due to fluctuating density gradients is

$$\begin{aligned}\overline{\rho}\left(\frac{\partial}{\partial t} + \overline{u}_j\frac{\partial}{\partial x_j}\right)\overline{\epsilon'} \;&=\; P_b^{\overline{\epsilon'}} + P_t^{\overline{\epsilon'}} + P_s^{\overline{\epsilon'}} + P_c^{\overline{\epsilon'}} \\ &\quad -D^{\overline{\epsilon'}} + T^{\overline{\epsilon'}}\,,\end{aligned} \tag{17}$$

where the buoyancy production, turbulent production, shear production, curvature production, turbulent destruction, and transport are

$$P_b^{\overline{\epsilon'}} = 2\,\overline{\nu}\,g_i\,\overline{\frac{\partial\rho'}{\partial x_j}\,\frac{\partial u_i'}{\partial x_j}} \to -2\,\overline{\nu}\,g\,\overline{\frac{\partial\rho'}{\partial x_j}\,\frac{\partial w'}{\partial x_j}}\,, \tag{18a}$$

$$P_t^{\overline{\epsilon'}} = -2\,\overline{\mu}\,\overline{\frac{\partial u_i'}{\partial x_k}\,\frac{\partial u_i'}{\partial x_j}\,\frac{\partial u_k'}{\partial x_j}}\,, \tag{18b}$$

$$\begin{aligned}P_s^{\overline{\epsilon'}} \;&=\; -2\,\overline{\mu}\left(\overline{\frac{\partial u_i'}{\partial x_k}\,\frac{\partial u_j'}{\partial x_k}} + \overline{\frac{\partial u_k'}{\partial x_i}\,\frac{\partial u_k'}{\partial x_j}}\right)\frac{\partial\overline{u}_i}{\partial x_j} \\ &\to\; -2\,\overline{\mu}\left(\overline{\frac{\partial u_i'}{\partial x_k}\,\frac{\partial w'}{\partial x_k}} + \overline{\frac{\partial u_k'}{\partial x_i}\,\frac{\partial u_k'}{\partial z}}\right)\frac{\partial\overline{u}_i}{\partial z}\,,\end{aligned} \tag{18c}$$

$$P_c^{\overline{\epsilon'}} = -\overline{\mu}\,\overline{u_j'\,\frac{\partial u_i'}{\partial x_k}}\,\frac{\partial^2\overline{u}_i}{\partial x_j\partial x_k} \to -\overline{\mu}\,\overline{w'\,\frac{\partial u_i'}{\partial z}}\,\frac{\partial^2\overline{u}_i}{\partial z^2}\,, \tag{18d}$$

$$D^{\overline{\epsilon'}} = 2\,\overline{\mu}\,\overline{\nu}\,\overline{\left(\frac{\partial^2 u_i'}{\partial x_j\partial x_k}\right)^2}\,, \tag{18e}$$

$$\begin{aligned}T^{\overline{\epsilon'}} \;&=\; -\frac{\partial}{\partial x_j}\left(\overline{\rho}\,\overline{\epsilon'\,u_j'} + 2\,\overline{\nu}\,\overline{\frac{\partial p'}{\partial x_k}\,\frac{\partial u_j'}{\partial x_k}} - \overline{\mu}\,\frac{\partial\overline{\epsilon'}}{\partial x_j}\right) \\ &\to\; -\frac{\partial}{\partial z}\left(\overline{\rho}\,\overline{\epsilon'\,w'} + 2\,\overline{\nu}\,\overline{\frac{\partial p'}{\partial x_k}\,\frac{\partial w'}{\partial x_k}} - \overline{\mu}\,\frac{\partial\overline{\epsilon'}}{\partial z}\right),\end{aligned} \tag{18f}$$

respectively (see Appendix C).

The analysis of the $\overline{\epsilon'}$ transport equation here provides the first budget of turbulent dissipation dynamics of Rayleigh–Taylor mixing. Figure 9 shows the dominant terms in the $\overline{\epsilon'}$ equation across the mixing layer: the production and destruction are qualitatively similar to the corresponding terms in the $\widetilde{E''}$ equation. All profiles approach zero at $z/h \approx \pm 0.7$, and there are less nonlocal effects than in the $\widetilde{E''}$ transport outside the layer boundaries. The density–vertical velocity gradient correlation in (18a) is negative-definite as $P_b^{\overline{\epsilon'}} \geq 0$. Turbulent production $P_t^{\overline{\epsilon'}}$ becomes the dominant production mechanism at late times when vortex stretching increases with increasing three-dimensionality and Reynolds number.

The mean advection $\overline{\rho}\,\overline{w}\partial\overline{\epsilon'}/\partial z$ is very small and is not shown. Similar to the turbulent kinetic energy, $\overline{\epsilon'}$ may be created by buoyancy forces and mean velocity gradients. However, $\overline{\epsilon'}$ may also be produced solely by

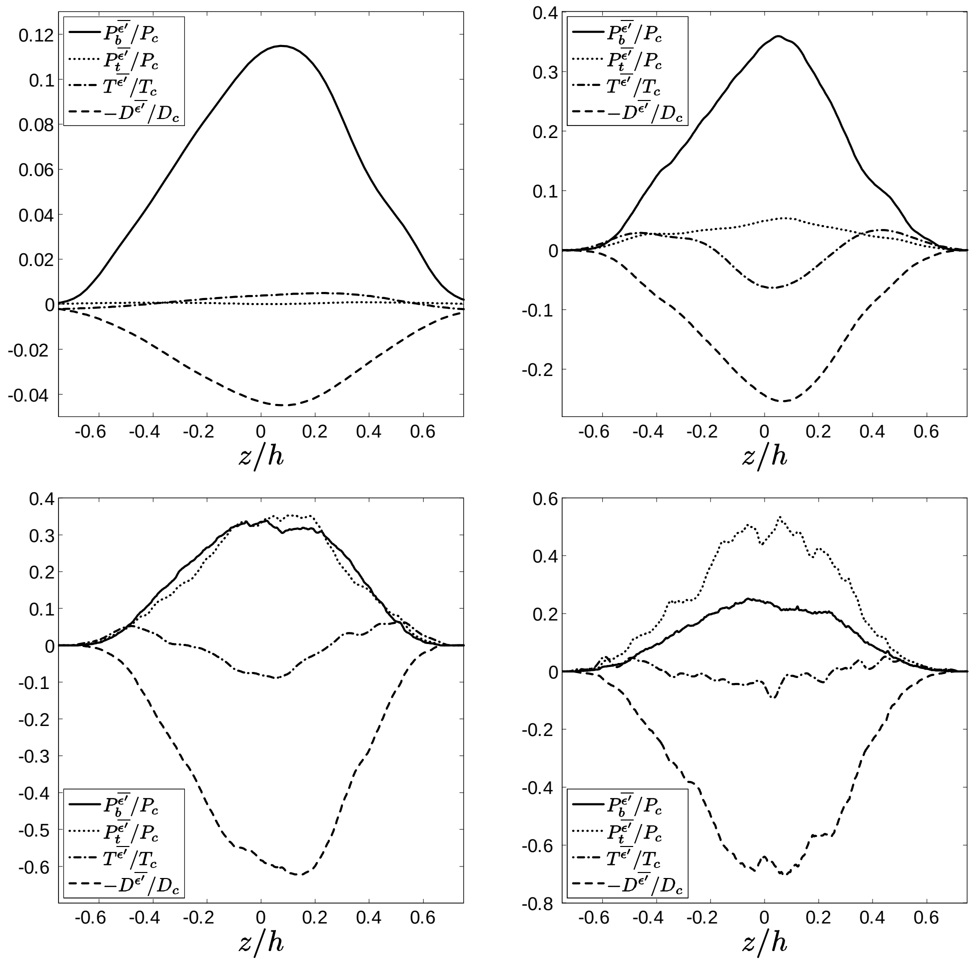

FIG. 9: Profiles of the dominant terms in the turbulent kinetic energy dissipation rate transport equation (17) normalized by $P_c = T_c = D_c = \rho_c u_c^2/t_c^2$ at $t/t_c = 5.13$ (top left), 12.6 (top right), 25.1 (bottom left), and 37.9 (bottom right).

turbulent fluctuations and by a term proportional to the second derivative of the mean velocity. Similar to $P_s^{\widetilde{E''}}$, the shear and curvature production $P_s^{\overline{\epsilon'}}$ and $P_c^{\overline{\epsilon'}}$ negligibly contribute to the total production and have no discernible structure.[7] Buoyancy production $P_b^{\overline{\epsilon'}}$ dominates at early times, but diminishes at later times (in constrast to $P_b^{\widetilde{E''}}$), as density fluctuations and their gradients are smoothed by the mixing. Turbulent production $P_t^{\overline{\epsilon'}}$ is nearly negligible until $t/t_c \approx 12.6$ when the transition to a fully three-dimensional mixing layer begins.[1,11] By $t/t_c \approx 25.1$, $P_t^{\overline{\epsilon'}}$ becomes the dominant production. Unlike in turbulent kinetic energy transport, these profiles are still changing between $t/t_c = 25.1$ and 37.9.

Turbulent destruction occurs primarily within the mixing layer core and only becomes significant when three-dimensional, turbulent fluctuations form after $t/t_c \approx 12.6$. The conservative transport of $\overline{\epsilon'}$ described by $T^{\overline{\epsilon'}}$ is similar to that of $\widetilde{E''}$: $\overline{\epsilon'}$ is transported away from the turbulent core approximately down-gradient. The profile rapidly increases between $t/t_c = 5.13$ and 12.6, and does not change significantly in magnitude from $t/t_c = 12.6$ to 37.9. The profiles have maxima near the layer edges $z/h = \pm 0.5$ and approach zero well outside the layer near $z/h = \pm 0.7$.

Referring to the order of magnitude in Eq. (B4), buoyancy production, turbulent production, turbulent destruction, and transport can be estimated at late times as $P_b^{\overline{\epsilon'}}/P_c \sim \left(\rho_{rms} g u_h^2/h\right)/P_c \sim 0.13$, $P_t^{\overline{\epsilon'}}/P_c \sim D^{\overline{\epsilon'}}/D_c \sim \rho_0 u_h^4/(2\lambda h D_c) \sim 0.58$, and $T^{\overline{\epsilon'}}/T_c \sim \rho_0 u_h^4/\left(2h^2 T_c\right) \sim 0.04$, in good agreement with the profiles in Fig. 9. The production and destruction rates are assumed to evolve on the time scale λ/u_h, so that $P_t^{\overline{\epsilon'}} \sim D^{\overline{\epsilon'}} \sim \overline{\rho}\overline{\epsilon'}/(\lambda/u_h)$.

V. SCALAR TURBULENT FLOW STRUCTURE

Turbulent transport within the Rayleigh–Taylor mixing layer was investigated above by considering the budgets of the exact $\widetilde{E''}$ and $\overline{\epsilon'}$ transport equations. Modeled evolution equations for these quantities are sufficient to construct an $\widetilde{E''}$-$\overline{\epsilon'}$ model based on the turbulent viscos-

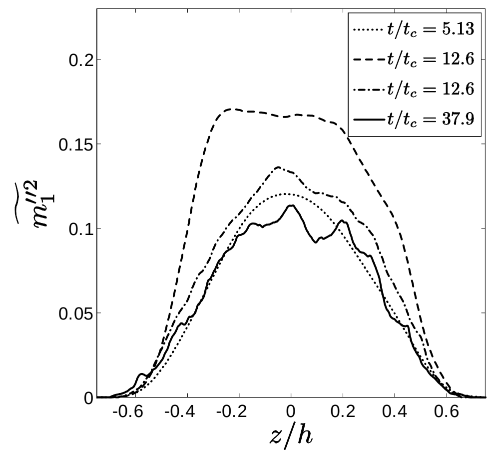

FIG. 10: Profiles of the heavy-fluid mass fraction variance $\widetilde{m_1''^2}$ at various dimensionless times.

ity $\nu_t \propto \left(\widetilde{E''}\right)^2/\overline{\epsilon'}$. In order to predict *molecular mixing dynamics*, additional scalar transport equations must be included for a mixing 'progress variable', such as the mass fraction variance and its dissipation rate. In scalar mixing and reacting flows, a transport equation for the mass fraction (or volume fraction) variance, and possibly its dissipation rate, are evolved[30]; the dissipation rate is often modeled algebraically.[31,32]

A. Heavy-fluid mass fraction variance transport

1. *Heavy-fluid mass fraction variance*

As the difference between the heavy-fluid volume fraction variance $\overline{f_1'^2}$ and mass fraction variance $\widetilde{m_1''^2}$ remains $< 3\%$ for the flow considered here, the difference between the budgets of the $\overline{f_1'^2}$ and $\widetilde{m_1''^2}$ transport equations is negligible. The profiles of $\widetilde{m_1''^2}$ in Fig. 10 are peaked near $z/h \approx 0$, exhibit moderate growth at early times up to $t/t_c = 12.6$, and then rapidly decrease for $t/t_c > 12.6$. The profile at $t/t_c = 12.6$ exhibits the most asymmetry across the layer. The growth and eventual decrease of heavy-fluid mass fraction variance is related to the growth and eventual decrease of density variance $\overline{\rho'^2}$, as reflected in the initial decrease followed by increase of the center plane molecular mixing parameter $\theta(z = 0)$ [see Eq. (32) and Fig. 16 in Ref. 1].

2. *Turbulent production, dissipation, and transport*

The heavy-fluid mass fraction variance transport equation is

$$\overline{\rho}\left(\frac{\partial}{\partial t} + \widetilde{u}_j\,\frac{\partial}{\partial x_j}\right)\widetilde{m_1''^2} = P^{\widetilde{m_1''^2}} - D^{\widetilde{m_1''^2}} + T^{\widetilde{m_1''^2}}\,, \quad (19)$$

where the mean production, turbulent dissipation, and transport are

$$P^{\widetilde{m_1''^2}} = -2\,\overline{\rho}\,\widetilde{m_1''\,u_j''}\,\frac{\partial\widetilde{m}_1}{\partial x_j} \to -2\,\overline{\rho}\,\widetilde{m_1''\,w''}\,\frac{\partial\widetilde{m}_1}{\partial z}\,, \quad (20a)$$

$$D^{\widetilde{m_1''^2}} = 2\,\overline{\rho}\,\widetilde{\chi''} = 2\,\overline{D}\;\overline{\rho\left(\frac{\partial m_1''}{\partial x_j}\right)^2}\,, \quad (20b)$$

$$\begin{aligned} T^{\widetilde{m_1''^2}} &= -\frac{\partial}{\partial x_j}\left(\overline{\rho}\,\widetilde{m_1''^2\,u_j''} - \overline{\rho}\,\overline{D}\,\frac{\partial\widetilde{m_1''^2}}{\partial x_j}\right) \quad (20c)\\ &\to -\frac{\partial}{\partial z}\left(\overline{\rho}\,\widetilde{m_1''^2\,w''} - \overline{\rho}\,\overline{D}\,\frac{\partial\widetilde{m_1''^2}}{\partial z}\right), \end{aligned}$$

respectively.[30,31] The terms in the mass fraction variance transport equation shown in Fig. 11 exhibit a generally similar production, dissipation, and transport structure as in the $\widetilde{E''}$ and $\overline{\epsilon'}$ equations. While the terms contributing to the $\widetilde{E''}$ and $\overline{\epsilon'}$ budgets generally *grow*, those contributing to the $\widetilde{m_1''^2}$ budget *decay* as mixing progresses and smooths mass fraction fluctuations. Late-time oscillations in the production and transport are due to oscillations in the mean field gradients.

The mean advection $\overline{\rho}\widetilde{w}\partial\widetilde{m_1''^2}/\partial z$ is very small and is not shown. At early times before the onset of three-dimensional dynamics, the mixing layer directly entrains pockets of pure fluid with little mixing, and therefore $P^{\widetilde{m_1''^2}}$ is large for $t/t_c \leq 12.6$. This can also be seen in the evolution of the mass fraction–vertical velocity correlation coefficient $R_{\widetilde{m_1''\,w''}} = \widetilde{m_1''\,w''}/\sqrt{\widetilde{m_1''^2}\widetilde{w''^2}}$ on the center plane of the mixing layer, shown in Fig. 3.63 of Ref. 7. Combining the large entrainment of fluid into the mixing layer (where $R_{\widetilde{m_1''\,w''}} \to 1$ at $t/t_c \approx 5.13$) and the large gradient of $\widetilde{m}_1$ at early times, the total production of $\widetilde{m_1''^2}$ is relatively large for $t/t_c \leq 12.6$. At later times, the correlation coefficient relaxes to $R_{\widetilde{m_1''\,w''}} \approx 0.75$ and the gradient of $\widetilde{m}_1$ scales as h^{-1}. Accordingly, the production of mass fraction variance decreases with time.

The production of $\widetilde{m_1''^2}$ corresponds to the entrainment of unmixed fluid into the mixing layer, which increases $\widetilde{m_1''^2}$. The dissipation of $\widetilde{m_1''^2}$ corresponds to molecular diffusion of each fluid species into the other, homogenizing the fluid within the mixing layer, thereby decreasing $\widetilde{m_1''^2}$. The heavy-fluid mass fraction variance dissipation rate $\widetilde{\chi''}$ determines the mixing rate. Turbulent dissipation of $\widetilde{m_1''^2}$ primarily occurs within the turbulent core. Larger turbulent fluctuations increase the local strain rates in the vicinity of the interface, thereby increasing local mass fraction gradients. The dissipation increases in time and begins to decrease for $t/t_c > 25.1$. The structure of the transport of $\widetilde{m_1''^2}$ is qualitatively

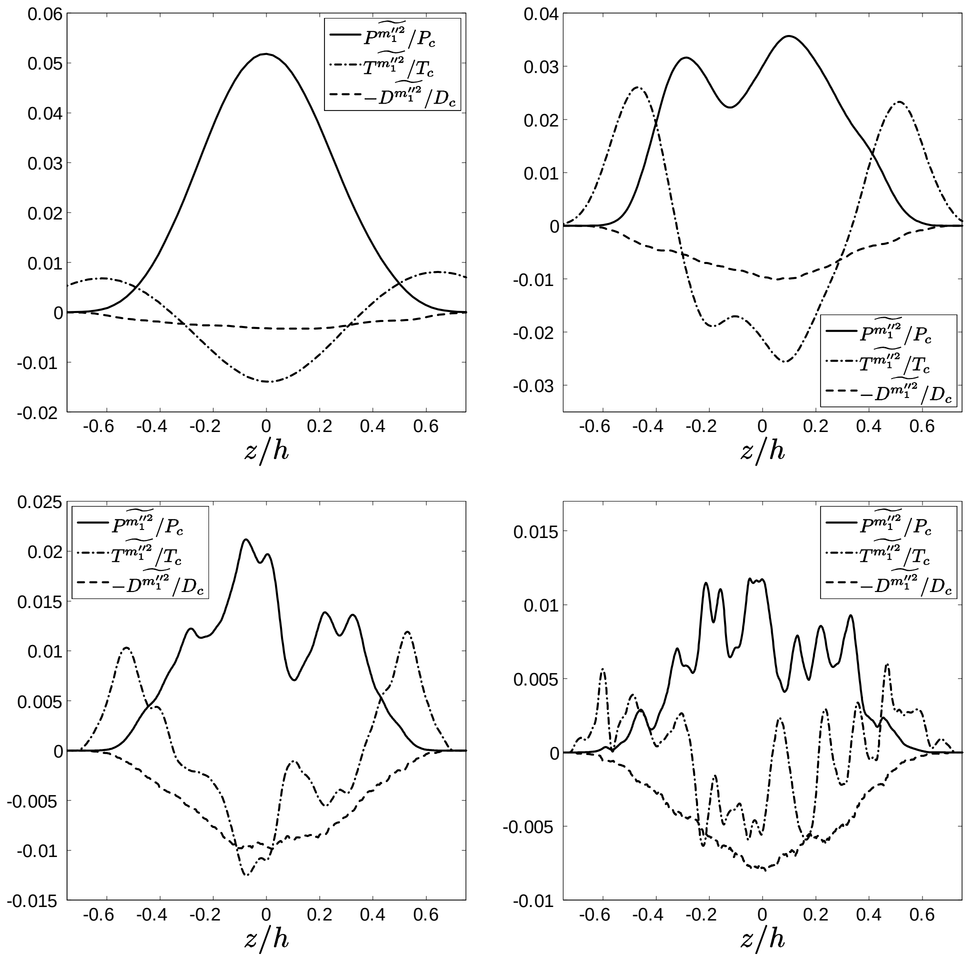

FIG. 11: Profiles of the terms in the heavy-fluid mass fraction variance transport equation (19) normalized by $P_c = T_c = D_c = \rho_c/t_c$ at $t/t_c = 5.13$ (top left), 12.6 (top right), 25.1 (bottom left), and 37.9 (bottom right).

similar to that of $\widetilde{E''}$ and $\overline{\epsilon'}$. However, the magnitude of $T^{\widetilde{m_1''^2}}$ increases initially, and then decreases with time. The total heavy-fluid mass fraction variance flux can be decomposed into its turbulent and diffusive components, $F_t^{\widetilde{m_1''^2}} = \overline{\rho}\widetilde{m_1''^2 w''}$ and $F_d^{\widetilde{m_1''^2}} = -\overline{\rho}\overline{D}\partial\widetilde{m_1''^2}/\partial z$, respectively. The diffusive flux is nearly zero.[7]

Referring to the order of magnitude in Eq. (B5), mean production, turbulent dissipation, and transport can be estimated at late times as (with $\Delta m \sim 1$) $P^{\widetilde{m_1''^2}}/P_c \sim (2\rho_0 m_{rms} \Delta m u_h/h)/P_c \sim 0.003$ and $D^{\widetilde{m_1''^2}}/D_c \sim T^{\widetilde{m_1''^2}}/T_c \sim \left(\rho_0 m_{rms}^2 u_h/\lambda_m\right)/D_c \sim 0.003$, in good agreement with the profiles in Fig. 11.

B. Heavy-fluid mass fraction variance dissipation rate transport

1. *Heavy-fluid mass fraction variance dissipation rate*

The heavy-fluid mass fraction variance dissipation rate

$$\widetilde{\chi''} = \overline{D}\,\overline{\left(\frac{\partial m_1''}{\partial x_j}\right)^2} \tag{21}$$

is shown in Fig. 12. Similar to $\widetilde{m_1''^2}$ and $D^{\widetilde{m_1''^2}}$, $\widetilde{\chi''}$ increases in time and begins to decrease for $t/t_c > 25.1$ as the mixing of the fluids reduces gradients of the fluctuating heavy-fluid mass fraction. The profile is asymmetric at $t/t_c = 5.13$, becoming more symmetric about the center plane subsequently. At late-time, $\widetilde{\chi''} t_c \sim m_{rms}^2 u_h t_c/(2\lambda_m) \sim 0.003$, in good agreement with the profile in Fig. 12.

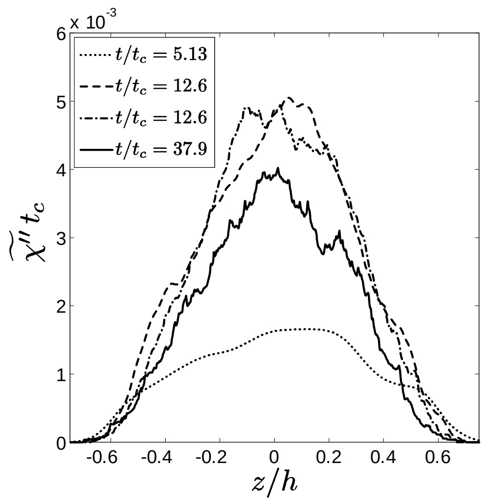

FIG. 12: Profiles of the heavy-fluid mass fraction variance dissipation rate $\widetilde{\chi''}$ normalized by $1/t_c$ at various dimensionless times.

2. Turbulent production, destruction, and transport

The heavy-fluid mass fraction variance dissipation rate transport equation is

$$\overline{\rho}\left(\frac{\partial}{\partial t}+\widetilde{u}_j\,\frac{\partial}{\partial x_j}\right)\widetilde{\chi''} = P_m^{\widetilde{\chi''}} + P_t^{\widetilde{\chi''}} + P_s^{\widetilde{\chi''}} + P_c^{\widetilde{\chi''}} - D^{\widetilde{\chi''}} + T^{\widetilde{\chi''}} , \tag{22}$$

where the mean field production, turbulent production, shear production, curvature, turbulent destruction, and transport are

$$P_m^{\widetilde{\chi''}} = -2\,\overline{D}\,\overline{\rho\,\frac{\partial m_1''}{\partial x_i}\,\frac{\partial u_j''}{\partial x_i}}\,\frac{\partial \widetilde{m}_1}{\partial x_j} \rightarrow -2\,\overline{D}\,\overline{\rho\,\frac{\partial m_1''}{\partial x_i}\,\frac{\partial w''}{\partial x_i}}\,\frac{\partial \widetilde{m}_1}{\partial z}\,, \tag{23a}$$

$$P_t^{\widetilde{\chi''}} = -2\,\overline{D}\,\overline{\rho\,\frac{\partial m_1''}{\partial x_i}\,\frac{\partial m_1''}{\partial x_j}\,\frac{\partial u_j''}{\partial x_i}}\,, \tag{23b}$$

$$P_s^{\widetilde{\chi''}} = -2\,\overline{D}\,\overline{\rho\,\frac{\partial m_1''}{\partial x_i}\,\frac{\partial m_1''}{\partial x_j}}\,\frac{\partial \widetilde{u}_j}{\partial x_i} \rightarrow -2\,\overline{D}\,\overline{\rho\,\frac{\partial m_1''}{\partial z}\,\frac{\partial m_1''}{\partial x_j}}\,\frac{\partial \widetilde{u}_j}{\partial z}\,, \tag{23c}$$

$$P_c^{\widetilde{\chi''}} = -2\,\overline{D}\,\overline{\rho\,u_j''\,\frac{\partial m_1''}{\partial x_i}}\,\frac{\partial^2 \widetilde{m}_1}{\partial x_i \partial x_j} \rightarrow -2\,\overline{D}\,\overline{\rho\,w''\,\frac{\partial m_1''}{\partial z}}\,\frac{\partial^2 \widetilde{m}_1}{\partial z^2}\,, \tag{23d}$$

$$D^{\widetilde{\chi''}} = 2\,\overline{D}^2\,\overline{\rho\left(\frac{\partial^2 m_1''}{\partial x_i \partial x_j}\right)^2}\,, \tag{23e}$$

$$T^{\widetilde{\chi''}} = -\frac{\partial}{\partial x_j}\left(\overline{\rho}\,\widetilde{\chi''\,u_j''} - \overline{\rho}\,\overline{D}\,\frac{\partial \widetilde{\chi''}}{\partial x_j}\right) \rightarrow -\frac{\partial}{\partial z}\left(\overline{\rho}\,\widetilde{\chi''\,w''} - \overline{\rho}\,\overline{D}\,\frac{\partial \widetilde{\chi''}}{\partial z}\right), \tag{23f}$$

respectively.[30,33–35] With suitably modeled equations for $\widetilde{E''}$, $\overline{\epsilon'}$, $\widetilde{m_1''^2}$, and $\widetilde{\chi''}$, a four-equation model describing Rayleigh–Taylor instability-generated turbulence and mixing can be constructed.

The dominant terms in the heavy-fluid mass fraction variance dissipation rate equation are shown in Fig. 13, where buoyancy and turbulent production are the primary production mechanisms of $\widetilde{\chi''}$ within the mixing layer core. The overall structure of the terms at the first time is quite different from that at subsequent times. The mean advection $\overline{\rho}\widetilde{w}\partial\widetilde{\chi''}/\partial z$ is very small and is not shown. As for the previous transport equations, the shear production $P_s^{\widetilde{\chi''}}$ is negligible compared to the other production mechanisms. The curvature production $P_c^{\widetilde{\chi''}}$ is larger in magnitude at early times when the mixing layer is small and $\partial^2\widetilde{m}_1/\partial z^2$ is large at $|z/h| \approx 0.5$ ($P_c^{\widetilde{\chi''}}$ is always negligible compared with $P_m^{\widetilde{\chi''}}$).[7] The mean production decreases in time as both the mass fraction fluctuations and mean mass fraction gradient decrease with progressive mixing; however, the total contribution to the production of $\widetilde{\chi''}$ remains approximately constant, as in turbulent premixed combustion.[34] For $t/t_c \gtrsim 9$, turbulent production becomes the dominant production mechanism (as in $\overline{\epsilon'}$ transport). Fluctuating velocity gradients strain concentration gradients, increasing the total interfacial surface area available for mass diffusion and increasing concentration gradients. These combined mechanisms result in increased rates of molecular diffusion and mixing.

The destruction of $\widetilde{\chi''}$ by molecular diffusion, $D^{\widetilde{\chi''}}$, remains small until the mixing layer begins to develop significant velocity fluctuations at $t/t_c \approx 9$. Similar to $D^{\widetilde{m_1''^2}}$, $D^{\widetilde{\chi''}}$ increases rapidly in time and eventually decreases for $t/t_c > 25.1$. As the mixing layer develops, $P_m^{\widetilde{\chi''}}$ decreases in magnitude, while $P_t^{\widetilde{\chi''}}$ and $D^{\widetilde{\chi''}}$ increase. Similar to the transport terms of $\widetilde{E''}$, $\overline{\epsilon'}$, and $\widetilde{m_1''^2}$, $\widetilde{\chi''}$ is transferred away from the turbulent core approximately down-gradient. However, the relative role of turbulent transport in the dynamics of $\widetilde{\chi''}$ is less important than in the previously considered transport equations. The individual flux contributions to $T^{\widetilde{\chi''}}$ can be decomposed into their turbulent and diffusive fluxes, $F_t^{\widetilde{\chi''}} = \overline{\rho}\widetilde{\chi'' w''}$ and $F_d^{\widetilde{\chi''}} = -\overline{\rho}\overline{D}\partial\widetilde{\chi''}/\partial z$, respectively. The diffusive flux is nearly zero at all times.[7]

Referring to the order of magnitude in Eq. (B6), turbulent production and destruction can be estimated at late times as $P_t^{\widetilde{\chi''}}/P_c \sim D^{\widetilde{\chi''}}/D_c \sim \rho_0 m_{rms}^2 u_h^2/\left(2\lambda_m^2 P_c\right) \sim 0.002$, in good agreement with the profiles in Fig. 13.

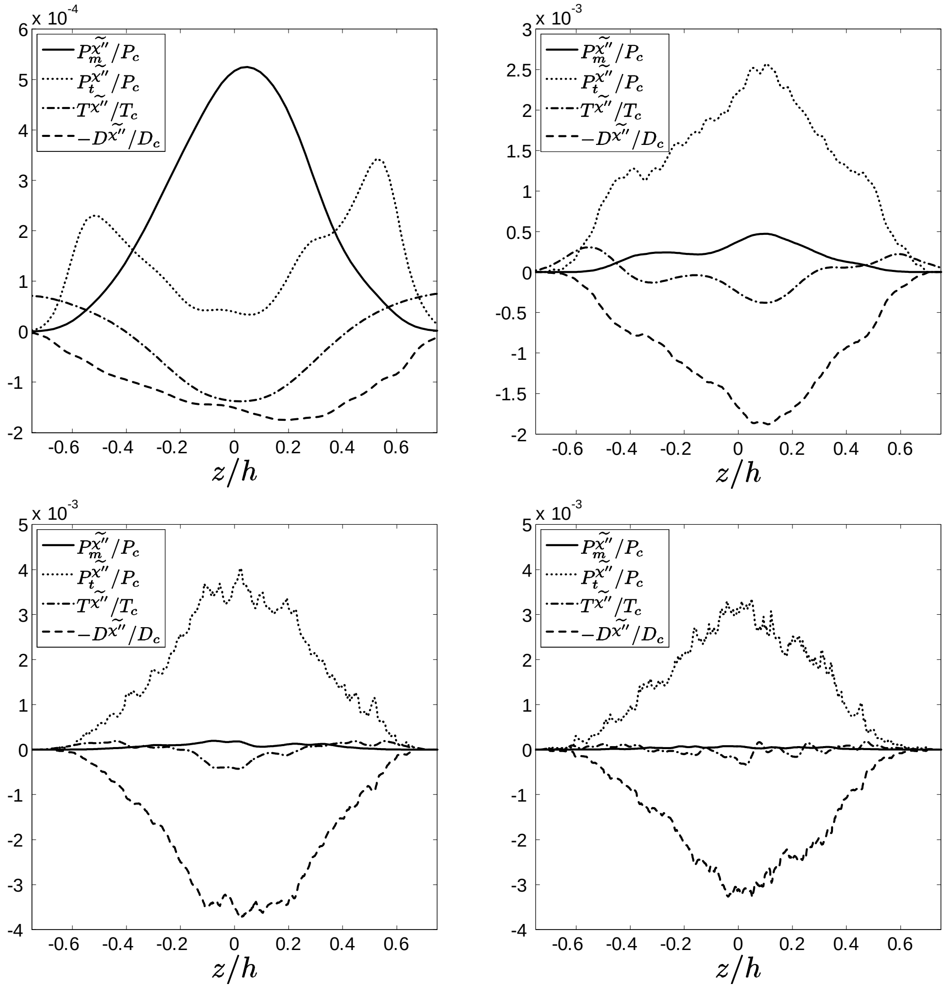

FIG. 13: Profiles of the dominant terms in the heavy-fluid mass fraction variance dissipation rate transport equation (22) normalized by $P_c = T_c = D_c = \rho_c/t_c^2$ at $t/t_c = 5.13$ (top left), 12.6 (top right), 25.1 (bottom left), and 37.9 (bottom right).

Here, the production and destruction rates are assumed to evolve on the time scale λ_m/u_h, so that $P_t^{\widetilde{\chi''}} \sim D^{\widetilde{\chi''}} \sim \overline{\rho}\widetilde{\chi''}/(\lambda_m/u_h)$.

VI. PRODUCTION AND DISSIPATION INTEGRALS, AND PRODUCTION-TO-DISSIPATION (DESTRUCTION) RATIOS

The integrated energy balances corresponding to the mechanical and scalar turbulent transport equations are discussed here, together with the production-to-dissipation (or destruction) ratios corresponding to each equation. Figure 14 shows the evolution of the production and dissipation integrated over the domain, $P^\phi(t) = \frac{1}{L_z}\int_{-L_z/2}^{L_z/2} P^\phi(z,t)dz$ and $D^\phi(t) = \frac{1}{L_z}\int_{-L_z/2}^{L_z/2} D^\phi(z,t)dz$, and Fig. 15 shows the second-order turbulence quantities, $\widetilde{E''}(t)$, $\overline{\epsilon'}(t)$, $\widetilde{m_1''^2}(t)$, and $\widetilde{\chi''}(t)$, similarly integrated over the domain. Figure 16 shows the production-to-dissipation (or destruction) ratios, and Fig. 17 shows their profiles across the mixing layer.

A. Turbulent kinetic energy production-to-dissipation ratio

Figure 14 indicates that the buoyancy production begins to grow rapidly, with an increasing growth rate for $t/t_c \gtrsim 18$ as the flow transitions to a more three-dimensional state.[1] Its growth begins to slow for $t/t_c \gtrsim 30$. The growth of the dissipation is delayed in time compared to the buoyancy production and grows only modestly, reaching a value approximately two times smaller than $P_b^{\widetilde{E''}}$ at the latest times. The integrated shear production does not contribute to the kinetic energy budget. The evolution of $\widetilde{E''}(t)$ shown in Fig. 15 exhibits a rapid quadratic growth at the latest times ($t/t_c > 25.1$), as expected from the self-similar scaling $\widetilde{E''} \sim u_h^2/2 \sim 2\left(\alpha A g\right)^2 t^2$ (see Appendix B). The spatial integral of

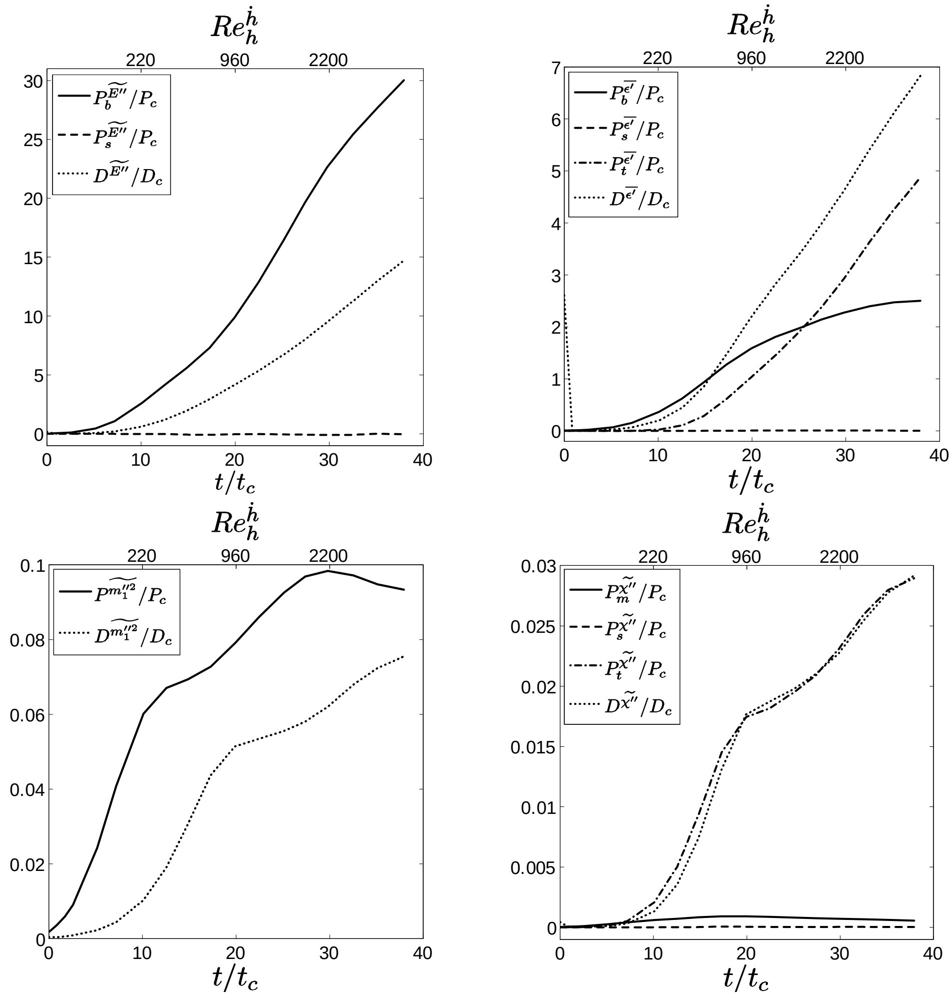

FIG. 14: Evolution of buoyancy and shear production, and dissipation integrals normalized by $P_c = T_c = D_c = \rho_c u_c^2/t_c$ corresponding to the $\widetilde{E''}$ equation (top left), evolution of buoyancy, shear, and turbulent production, and destruction integrals normalized by $P_c = T_c = D_c = \rho_c u_c^2/t_c^2$ corresponding to the $\overline{\epsilon'}$ equation (top right), evolution of production and dissipation integrals normalized by $P_c = T_c = D_c = \rho_c/t_c$ corresponding to the $\widetilde{m_1''^2}$ equation (bottom left), and evolution of mean, shear and turbulent production, and destruction integrals normalized by $P_c = T_c = D_c = \rho_c/t_c^2$ corresponding to the $\widetilde{\chi''}$ equation (bottom right)

Eq. (B3) is $\frac{d}{dt}\left[\overline{\rho}\widetilde{E''}(t)\right] = P_b^{\widetilde{E''}}(t) + P_s^{\widetilde{E''}}(t) + \Pi^{\widetilde{E''}}(t) - D^{\widetilde{E''}}(t) \approx P_b^{\widetilde{E''}}(t) - D^{\widetilde{E''}}(t)$, representing a balance between terms of $\mathcal{O}(\rho_{rms} g u_h)$ and $\mathcal{O}(\rho_0 u_h^3/h)$: in the late-time self-similar regime, this is a balance between terms growing linearly as $2\alpha A \rho_{rms} g^2 t$ and $8\,(\alpha A)^2\,\rho_0 g^2 t$, respectively.

The departure of the production-to-dissipation ratio $P^{\widetilde{E''}}/D^{\widetilde{E''}}$ from unity (with $P^{\widetilde{E''}} = P_b^{\widetilde{E''}} + P_s^{\widetilde{E''}} \approx P_b^{\widetilde{E''}}$) shown in Fig. 16 indicates that turbulence statistics are rapidly changing with respect to the mean fields. At early times ($t/t_c < 12.6$), the ratio exhibits a large dynamic range. As the growth of the initial perturbations increases, $P^{\widetilde{E''}}/D^{\widetilde{E''}}$ rises until a peak value ≈ 5 is reached at $t/t_c \approx 6$. The maximum value corresponds to the nonlinear transition time, where secondary vortices begin to form in between rising and falling structures. The onset of nonlinear dynamics is correlated with the bifurcation of the pressure flux $\overline{p'w''}$ (see Fig. 19 in Appendix A). Following the onset of the transition at $t/t_c \approx 6$, the mixing eventually relaxes to an asymptotic state with

$$\frac{P^{\widetilde{E''}}}{D^{\widetilde{E''}}} = -\frac{\overline{w''}\,\frac{\partial \overline{p}}{\partial z}}{\overline{\rho}\,\overline{\epsilon'}} \approx \frac{g\,\overline{w''}}{\overline{\epsilon'}} \approx 2.0\,. \tag{24}$$

This relaxation occurs more rapidly until $t/t_c \approx 13$, after which the turbulence statistics begin to change more slowly. Referring to the scalings in Appendix B and to Fig. 7, $P^{\widetilde{E''}}/D^{\widetilde{E''}} \sim \Delta\overline{U}/\Delta\widetilde{E''} \sim (\rho_{rms}/\rho_0)\,Fr_h^{-2} \sim 1.5$ at the latest time, which is $\sim 25\%$ smaller than the numerical value. At asymptotically late times, $h \sim \alpha A g t^2$ and $u_h \sim 2\alpha A g t$ give the constant value $Fr_h \sim 2\sqrt{\alpha A}$, so that in a self-similar state in which $\rho_{rms}/\rho_0 = constant$, it follows that $P^{\widetilde{E''}}/D^{\widetilde{E''}} \sim (\rho_{rms}/\rho_0)(4\alpha A)^{-1} \approx 1.54$,

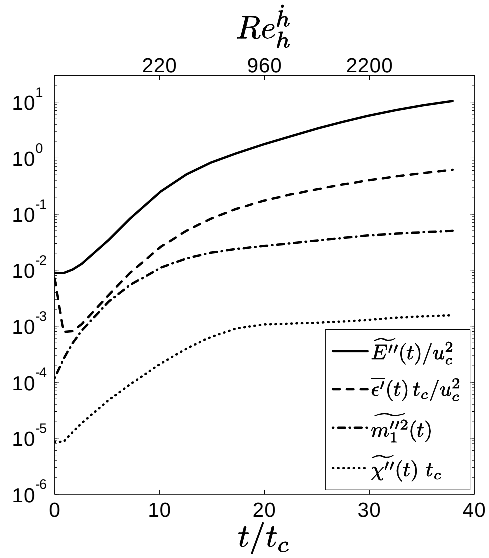

FIG. 15: Evolution of the turbulent kinetic energy per unit mass $\widetilde{E''}$ normalized by u_c^2, turbulent kinetic energy dissipation rate per unit mass $\overline{\epsilon'}$ normalized by u_c^2/t_c, heavy-fluid mass fraction variance $\widetilde{m_1''^2}$, and heavy-fluid mass fraction variance dissipation rate $\widetilde{\chi''}$ normalized by $1/t_c$.

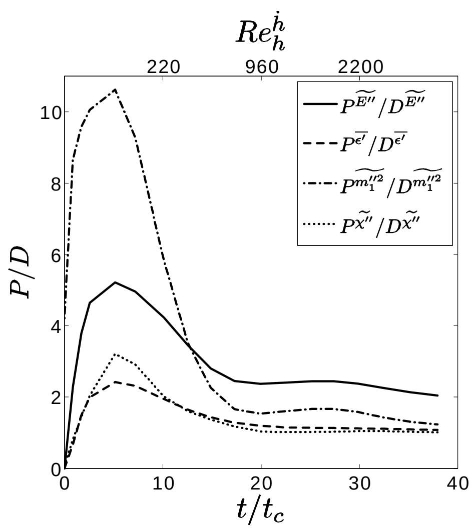

FIG. 16: Evolution of the production-to-dissipation ratios $P^{\widetilde{E''}}/D^{\widetilde{E''}}$ and $P^{\widetilde{m_1''^2}}/D^{\widetilde{m_1''^2}}$, and of the production-to-destruction ratios $P^{\overline{\epsilon'}}/D^{\overline{\epsilon'}}$ and $P^{\widetilde{\chi''}}/D^{\widetilde{\chi''}}$.

or $\sim$ 23% smaller than the numerical value. In wall-bounded flows, the *spatial* profile of $P^{\overline{E'}}/D^{\overline{E'}}$ versus the normalized wall coordinate[26] exhibits a qualitative structure similar to the *temporal* profile in Fig. 16, beginning at zero, rising rapidly to a maximum value as a result of the nonequilibrium flow dynamics in the vicinity of the wall, and then decreasing to a nearly constant value.

Figure 17 shows $P^{\widetilde{E''}}/D^{\widetilde{E''}}$, which is narrow and largest at the earliest time, decreases rapidly between $t/t_c = 5.13$ and 12.6, and does not change significantly between the last two times. At the latest time, the profile is approximately flat across the layer, approaching zero outside the layer boundaries at $z/h \approx \pm 0.65$; the profile broadens with time. These ratios were previously examined using DNS,[13] and were similar to the late-time profiles shown here, but larger in magnitude.

Two-equation turbulence modeling requires that the production-to-dissipation ratio remain close to unity, i.e., turbulent statistics vary slowly in time with respect to mean flow changes. This is one reason why standard $\overline{E'}$-$\overline{\epsilon'}$ models[36] are adequate for round jet flows with $P^{\overline{E'}}/D^{\overline{E'}} \approx 0.8$,[19] homogeneous shear flows with $P^{\overline{E'}}/D^{\overline{E'}} \approx 1.4$–$1.8$,[37,38] and shear-driven mixing layers with $P^{\overline{E'}}/D^{\overline{E'}} \approx 1.4$.[39] The Rayleigh–Taylor mixing layer here exhibits considerably larger ratios $P^{\widetilde{E''}}/D^{\widetilde{E''}} \approx$ 2–2.4. LES of a compressible, miscible, $A = 0.5$ Rayleigh–Taylor mixing layer also gave $P^{\widetilde{E''}}/D^{\widetilde{E''}} \approx$ 2–2.5.[40] Even larger values $P^{\widetilde{E''}}/D^{\widetilde{E''}} \approx 3.5$ were obtained from DNS of an $A = 0.01$, $\mathrm{Sc} = 1$ Rayleigh–Taylor mixing layer.[13] The difference between the Rayleigh–Taylor and shear-driven production-to-dissipation ratios is attributable to the distinct production mechanisms: turbulent kinetic energy is created by mean density gradients rather than by mean velocity gradients.

B. Turbulent kinetic energy dissipation rate production-to-destruction ratio

The evolution of the integrated production and destruction is shown in Fig. 14. Buoyancy production dominates at early times $t/t_c < 25.1$, and becomes less important as the Reynolds number increases; $P^{\overline{\epsilon'}} \approx P_b^{\overline{\epsilon'}} + P_t^{\overline{\epsilon'}}$. Turbulent production and destruction are small until the layer transitions to a nonlinear, three-dimensional phase at $t/t_c \approx 13$. Specifically, $P_t^{\overline{\epsilon'}} \approx 0$ for $t/t_c < 13$, increasing rapidly thereafter. Eventually, $P_t^{\overline{\epsilon'}}$ exceeds $P_b^{\overline{\epsilon'}}$ for $t/t_c > 25.1$; at the end of the simulation, $P_t^{\overline{\epsilon'}}$ exceeds $P_b^{\overline{\epsilon'}}$ by a factor of ≈ 2. While $P_t^{\overline{\epsilon'}}$ increases steadily, $P_b^{\overline{\epsilon'}}$ attains a nearly steady value at the latest time. For $t/t_c < 19$, $P_b^{\overline{\epsilon'}} \gtrsim D^{\overline{\epsilon'}}$ and for $t/t_c > 19$, $D^{\overline{\epsilon'}} \gg P_b^{\overline{\epsilon'}}$. The spatial integral of Eq. (B4) is $\frac{d}{dt}\left[\overline{\rho}\overline{\epsilon'}(t)\right] = P_b^{\overline{\epsilon'}}(t) + P_t^{\overline{\epsilon'}}(t) + P_s^{\overline{\epsilon'}}(t) + P_c^{\overline{\epsilon'}}(t) + \Pi^{\overline{\epsilon'}}(t) - D^{\overline{\epsilon'}}(t) \approx P_b^{\overline{\epsilon'}}(t) + P_t^{\overline{\epsilon'}}(t) - D^{\overline{\epsilon'}}(t)$, representing a balance between terms of $\mathcal{O}(\overline{\nu}\rho_{rms} g u_h/\lambda^2) \sim \mathcal{O}(\rho_{rms} g u_h^2/h)$, $\mathcal{O}(\overline{\mu} u_h^3/\lambda^3) \sim \mathcal{O}\left[\rho_0 u_h^4/(2\lambda h)\right]$, and $\mathcal{O}\left[\overline{\mu}\overline{\nu} u_h^2/(\lambda^2\delta^2)\right] \sim \mathcal{O}\left[\rho_0 u_h^4/(2\lambda h)\right]$, respectively: in the self-similar regime, this is a balance between terms $4\rho_{rms}\alpha A g^2$, $8^{3/2}\overline{\mu}\left(\alpha A g\right)^3 \left(t/\overline{\nu}\right)^{3/2}$, and $8^{3/2}\overline{\mu}\left(\alpha A g\right)^3 \left(t/\overline{\nu}\right)^{3/2}$, respectively. The buoyancy production indeed begins to change very slowly at the latest times, in accordance with the scaling prediction. The evolution of $\overline{\epsilon'}(t)$ shown in Fig. 15 exhibits linear growth at the latest times, as expected from the self-similar

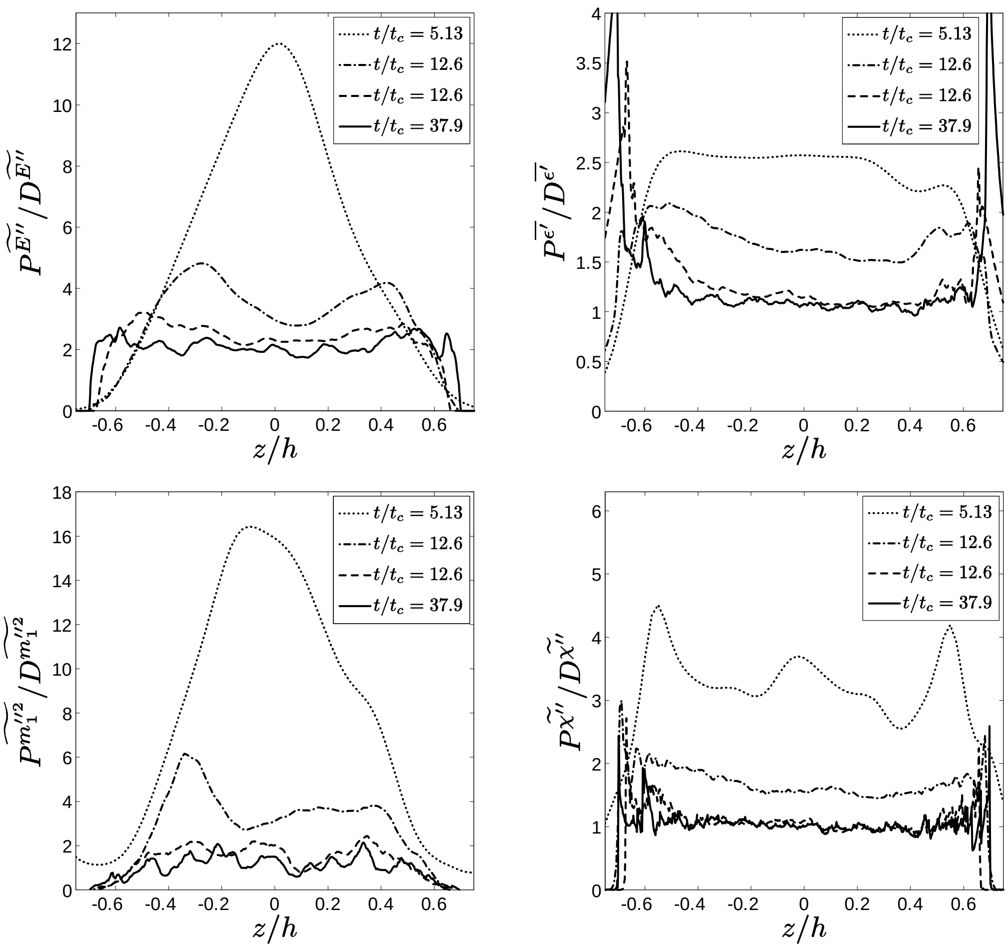

FIG. 17: Profiles of $P^{\widetilde{E''}}/D^{\widetilde{E''}}$ (top left), $P^{\overline{\epsilon'}}/D^{\overline{\epsilon'}}$ (top right), $P^{\widetilde{m_1''^2}}/D^{\widetilde{m_1''^2}}$ (bottom left), and $P^{\widetilde{\chi''}}/D^{\widetilde{\chi''}}$ (bottom right) at various dimensionless times.

scaling $\overline{\epsilon'} \sim u_h^3/(2h) \sim 4\,(\alpha A g)^2\, t$. The scaling arguments in Appendix B suggest $\mathrm{Re}_\lambda^2/15 \sim \mathrm{Re}_h \sim 2\mathrm{Re}_t = 2\left(\widetilde{E''}\right)^2/\left(\overline{\epsilon'}\overline{\nu}\right) \sim 2\,(\alpha A g)^2\, t^3/\overline{\nu}$, consistent with the more rapid growth for $t/t_c > 25.1$ seen in Fig. 2 of Ref. 1. Note that $P_t^{\overline{\epsilon'}}(t)$ and $D^{\overline{\epsilon'}}(t)$ grow at the same rate.

The ratio $P^{\overline{\epsilon'}}/D^{\overline{\epsilon'}}$ shown in Fig. 16 indicates that the turbulence is highly nonstationary before $t/t_c \approx 19$; after $t/t_c \approx 19$,

$$\frac{P^{\overline{\epsilon'}}}{D^{\overline{\epsilon'}}} = -\frac{\frac{g}{\overline{\rho}}\,\overline{\frac{\partial \rho'}{\partial x_j}\frac{\partial w'}{\partial x_j}} + \overline{\frac{\partial u_i'}{\partial x_k}\frac{\partial u_i'}{\partial x_j}\frac{\partial u_k'}{\partial x_j}}}{\overline{\nu}\,\overline{\left(\frac{\partial^2 u_i'}{\partial x_j \partial x_k}\right)^2}} \approx 1.1\,. \tag{25}$$

Using the late-time scalings, $P^{\overline{\epsilon'}}/D^{\overline{\epsilon'}} \sim 2\,(\rho_{rms}/\rho_0)\, Fr_h^{-2}\,(\lambda/h) + 1 \sim \left(P^{\widetilde{E''}}/D^{\widetilde{E''}}\right)(2\lambda/h) + 1 \sim 1.23$ at the latest time ($\sim 12\%$ larger than the numerical value). The profiles of $P^{\overline{\epsilon'}}/D^{\overline{\epsilon'}}$ shown in Fig. 17 are approximately constant within the core $z/h \in [-0.3, 0.3]$ at all times, and have very large peaks outside of the layer boundaries at $z/h \approx \pm 0.65$ at the latest two times. The ratio decreases between $t/t_c = 5.13$ and 12.6, and does not change significantly between the last two times (similar to $P^{\widetilde{E''}}/D^{\widetilde{E''}}$). Unlike $P^{\widetilde{E''}}/D^{\widetilde{E''}}$, the profiles do not significantly broaden with time.

C. Heavy-fluid mass fraction variance production-to-dissipation ratio

The production of $\widetilde{m_1''^2}$ is driven by the mixing layer expansion and entrainment of unmixed fluid. The destruction rate of $\widetilde{m_1''^2}$ depends on the turbulent fluctuations to create the necessary surface area required for molecular diffusion to mix the constituent fluids. Figure 14 shows that the production of $\widetilde{m_1''^2}$ exhibits rapid growth and is larger than $D^{\widetilde{m_1''^2}}$ at early times ($t/t_c < 10$); $P^{\widetilde{m_1''^2}}$ grows less rapidly for $t/t_c > 13$, attains a maximum at $t/t_c \approx 30$, and then slowly decreases. The dissipation $D^{\widetilde{m_1''^2}}$ also grows rapidly at early times, with a slower growth for $t/t_c > 19$. This evolution of the production and dissipation leads to the evolution of $\widetilde{m_1''^2}$ in Fig. 15, where the mass fraction variance approaches a nearly constant (but slightly increasing) value near the end of the simulation. This is consistent with the nearly constant late-time molecular mixing rate θ [Eq. (32) and Fig. 16 of Ref. 1], which follows from $\overline{\rho'^2} = (\Delta\rho)^2\,\overline{f_1'^2} \approx (\Delta\rho)^2\,\widetilde{m_1''^2} \sim$ *constant* at late times. The spatial integral of Eq. (B5) is $\frac{d}{dt}\left[\overline{\rho}\widetilde{m_1''^2}(t)\right] = P^{\widetilde{m_1''^2}}(t) - D^{\widetilde{m_1''^2}}(t)$, representing a balance between terms of $\mathcal{O}(2\rho_0 m_{rms}\Delta m u_h/h)$ and $\mathcal{O}\left(\rho_0 m_{rms}^2 u_h/\lambda_m\right)$, respectively: in the self-similar regime, this is a balance between terms decaying as $2\rho_0 m_{rms}\Delta m/t$ and $\left(\rho_0 m_{rms}^2/t\right)\sqrt{\mathrm{Re}_h\mathrm{Sc}/12}$, respectively.

As three-dimensional turbulent structures develop within the mixing layer for $t/t_c > 19$,[1] the ratio shown in Fig. 16 approaches

$$\frac{P^{\widetilde{m_1''^2}}}{D^{\widetilde{m_1''^2}}} = -\frac{\widetilde{m_1''\,w''}\,\frac{\partial\widetilde{m}_1}{\partial z}}{\widetilde{\chi''}} \approx 1.25 \tag{26}$$

at the end of the simulation. Using the late-time scalings, $P^{\widetilde{m_1''^2}}/D^{\widetilde{m_1''^2}} \sim 2\Delta m\lambda_m/(h m_{rms}) \sim 1$ (25% smaller than the numerical value). Similar to $P^{\widetilde{E''}}/D^{\widetilde{E''}}$, $P^{\widetilde{m_1''^2}}/D^{\widetilde{m_1''^2}}$ shown in Fig. 17 is narrow and largest at the earliest time, with the ratio decreasing rapidly between $t/t_c = 5.13$ and 12.6, and not changing significantly between the last two times. At the latest time, the profile is approximately flat across the layer (though less flat compared to $P^{\widetilde{E''}}/D^{\widetilde{E''}}$ at the latest time), approaching zero outside of the layer boundaries at $z/h \approx \pm 0.6$. The production-to-dissipation ratios of the concentration variance were also previously examined,[13] were more symmetric than those shown here at the two earliest times, and were similar to the late-time profiles shown here.

D. Heavy-fluid mass fraction variance dissipation rate production-to-destruction ratio

The integrated production and destruction terms shown in Fig. 14 indicate that $P^{\widetilde{\chi''}} \gtrsim D^{\widetilde{\chi''}}$, where $P^{\widetilde{\chi''}} = P_m^{\widetilde{\chi''}} + P_t^{\widetilde{\chi''}} + P_s^{\widetilde{\chi''}} + P_c^{\widetilde{\chi''}} \approx P_m^{\widetilde{\chi''}} + P_t^{\widetilde{\chi''}}$. Both the production and destruction are nearly zero for $t/t_c \le 10$, grow rapidly thereafter until $t/t_c \approx 19$, and then grow more slowly. The very slow growth of $\widetilde{\chi''}(t)$ seen in Fig. 15 is consistent with the production slightly exceeding the dissipation for $t/t_c > 19$. The spatial integral of Eq. (B5) is $\frac{d}{dt}\left[\overline{\rho}\widetilde{\chi''}(t)\right] = P_m^{\widetilde{\chi''}}(t) + P_t^{\widetilde{\chi''}}(t) + P_s^{\widetilde{\chi''}}(t) + P_c^{\widetilde{\chi''}}(t) - D^{\widetilde{\chi''}}(t) \approx P_t^{\widetilde{\chi''}}(t) - D^{\widetilde{\chi''}}(t)$, representing a balance between terms both of $\mathcal{O}\left[\rho_0 m_{rms}^2 u_h^2/(2h\lambda)\right] \sim \mathcal{O}\left[\rho_0 m_{rms}^2 u_h^2\sqrt{\mathrm{Re}_h}/\left(2h^2\right)\right]$: in the self-similar regime, this is a balance between terms both decaying as $2^{3/2}\rho_0 m_{rms}^2\alpha A g/\sqrt{\overline{\nu}t}$.

Similar to the turbulent kinetic energy dissipation rate $\overline{\epsilon'}$, the total production is greater than the destruction until $t/t_c \approx 19$, after which $P^{\widetilde{\chi''}}/D^{\widetilde{\chi''}}$ in Fig. 16 remains

$$\frac{P^{\widetilde{\chi''}}}{D^{\widetilde{\chi''}}} = -\frac{\overline{\rho\,\frac{\partial m_1''}{\partial x_i}\,\frac{\partial m_1''}{\partial x_j}\,\frac{\partial u_j''}{\partial x_i}}}{\overline{D}\,\overline{\rho\left(\frac{\partial^2 m_1''}{\partial x_i\partial x_j}\right)^2}} \approx 1\,, \tag{27}$$

in agreement with the late-time scalings. The profiles of $P^{\widetilde{\chi''}}/D^{\widetilde{\chi''}}$ shown in Fig. 17 are approximately constant within the mixing layer core $z/h \in [-0.3, 0.3]$ at the latest three times, and have large peaks outside the layer boundaries at $z/h \approx \pm 0.65$ at the latest two times, where the nonequilibrium behavior is the strongest. As for all other production-to-dissipation (or destruction) ratios, the ratio decreases between $t/t_c = 5.13$ and 12.6, and does not change between the last two times (when the profiles are also very flat). The profiles do not significantly broaden with time.

VII. DISCUSSION AND CONCLUSIONS

Data from a $1152 \times 760 \times 1280$ direct numerical simulation of a Rayleigh–Taylor mixing layer[1,11] modeled after a water channel experiment[6] was used to systematically investigate the spatiotemporal dynamics of turbulent transport and mixing. The simulation had parameters and initial conditions approximating those in the experiment. The initial conditions were parametrized from an extensive set of experimental measurements of the flow field a short distance from the splitter plate, and were anisotropic.

Budgets of the mean vertical momentum and heavy-fluid mass fraction equations and of the turbulent kinetic energy, turbulent kinetic energy dissipation rate, heavy-fluid mass fraction variance, and heavy-fluid mass fraction variance dissipation rate equations were constructed as spanwise profiles across the layer. The relative importance of the terms was examined as a function of Reynolds number to elucidate scalar transport and mixing in Rayleigh–Taylor flow. Modeled transport equations for $\widetilde{\chi''}$ are used in premixed or partially-premixed combustion applications,[33–35] particularly when the mechanical-to-scalar time scale ratio (used in algebraic closures of $\widetilde{\chi''}$) is not constant or varies from flow to flow. This work presents the first budgets of the $\overline{\epsilon'}$, $\widetilde{m_1''^2}$, and $\widetilde{\chi''}$ transport equations for this type of flow, and aids prioritizing modeling efforts by identifying the important transport and mixing mechanisms.

The structure of the mean flow defined by Reynolds averaging the governing equations (1a)–(1c) was considered first. The mean vertical momentum equation reduces to a balance between the gravitational force, mean vertical pressure gradient, and vertical Reynolds stress gradient, corresponding to hydrostatic equilibrium with a total pressure given by the mean pressure, $\overline{p}$, plus the turbulent pressure $\overline{\rho}\widetilde{w''^2}$. The vertical velocity variance is the dominant Reynolds stress component, and Reynolds stress anisotropy persists to the latest times.[1]

The structure of the turbulent transport equations was also investigated. The turbulent kinetic energy and its dissipation rate grow and are peaked near the center plane of the mixing layer; the heavy-fluid mass fraction variance and its dissipation rate initially grow and then decrease as mixing progresses. The principal transport mechanisms are buoyancy and turbulent production, turbulent dissipation, and turbulent transport. The shear productions were negligible as the mean velocity and its gradients are very small. The pressure–dilatation correlation does not contribute to the budget. The mean flow and turbulence equations approximately reduce to

$$\overline{\rho}\, g \approx \frac{\partial}{\partial z}\left(\overline{p} + \overline{\rho}\, \widetilde{w''^2}\right), \tag{28}$$

$$\overline{\rho}\, \frac{\partial \widetilde{m}_1}{\partial t} \approx -\frac{\partial}{\partial z}\left(\overline{\rho}\, \widetilde{m_1'' w''}\right), \tag{29}$$

$$\begin{aligned} \overline{\rho}\, \frac{\partial \widetilde{E''}}{\partial t} \;\approx\; & -\overline{w''}\, \frac{\partial \overline{p}}{\partial z} - \overline{\rho}\, \widetilde{\epsilon''} \\ & -\frac{\partial}{\partial z}\left(\overline{\rho}\, \widetilde{E'' w''} + \overline{p' w''}\right), \end{aligned} \tag{30}$$

$$\begin{aligned} \overline{\rho}\, \frac{\partial \overline{\epsilon'}}{\partial t} \;\approx\; & -2\, \overline{\nu}\, g\, \overline{\frac{\partial \rho'}{\partial x_j}\, \frac{\partial w'}{\partial x_j}} - 2\, \overline{\mu}\, \overline{\frac{\partial u_i'}{\partial x_k}\, \frac{\partial u_i'}{\partial x_j}\, \frac{\partial u_k'}{\partial x_j}} \\ & -2\, \overline{\mu}\, \overline{\nu}\, \overline{\left(\frac{\partial^2 u_i'}{\partial x_j \partial x_k}\right)^2} \\ & -\frac{\partial}{\partial z}\left(\overline{\rho}\, \overline{\epsilon' w'} + 2\, \overline{\nu}\, \overline{\frac{\partial p'}{\partial x_k}\, \frac{\partial w'}{\partial x_k}}\right), \end{aligned} \tag{31}$$

$$\begin{aligned} \overline{\rho}\, \frac{\partial \widetilde{m_1''^2}}{\partial t} \;\approx\; & -2\, \overline{\rho}\, \widetilde{m_1'' w''}\, \frac{\partial \widetilde{m}_1}{\partial z} - 2\, \overline{\rho}\, \widetilde{\chi''} \\ & -\frac{\partial}{\partial z}\left(\overline{\rho}\, \widetilde{m_1''^2 w''}\right), \end{aligned} \tag{32}$$

$$\begin{aligned} \overline{\rho}\, \frac{\partial \widetilde{\chi''}}{\partial t} \;\approx\; & -2\, \overline{D}\, \overline{\rho\, \frac{\partial m_1''}{\partial x_i}\, \frac{\partial m_1''}{\partial x_j}\, \frac{\partial u_j''}{\partial x_i}} \\ & -2\, \overline{D}^2\, \overline{\rho \left(\frac{\partial^2 m_1''}{\partial x_i \partial x_j}\right)^2} - \frac{\partial}{\partial z}\left(\overline{\rho}\, \widetilde{\chi'' w''}\right). \end{aligned} \tag{33}$$

The terms in the transport equations retain the same qualitative structure across the layer, with the exception of the pressure flux contributions to the total turbulent kinetic energy and kinetic energy dissipation rate fluxes, which exhibit a change early in the evolution (a counter-gradient effect). The pressure flux contributing to turbulent kinetic energy transport is non-negligible and complex in behavior. A bifurcation was observed at the onset of nonlinear, secondary instabilities, where the pressure fluctuations transported $\widetilde{E''}$ down-gradient, away from the center plane at early times ($t/t_c \leq 7.19$). Following this transition ($t/t_c > 7.19$), the pressure flux opposed the down-gradient turbulent flux of $\widetilde{E''}$ within the mixing layer core ($|z/h| < 0.5$), but augmented the turbulent flux of $\widetilde{E''}$ outside the layer boundaries ($|z/h| > 0.5$).

Turbulent production in the $\overline{\epsilon'}$ equation eventually dominates buoyancy production, which begins to decrease at late times as density fluctuations are smoothed. The production and dissipation (or destruction) integrals for each transport equation, $\partial\phi_\alpha/\partial t \approx P_{\phi_\alpha} - D_{\phi_\alpha} + T_{\phi_\alpha}$, i.e., $\int_{-L_z/2}^{L_z/2} P_{\phi_\alpha} dz$ and $\int_{-L_z/2}^{L_z/2} D_{\phi_\alpha} dz$, were examined to elucidate the energy balance ($\int_{-L_z/2}^{L_z/2} T_{\phi_\alpha} dz \approx 0$ for conservative redistribution). The production-to-dissipation (or destruction) ratios corresponding to each transport equation are large at small times, decrease with time, and eventually approach nearly constant values. For $t/t_c \gtrsim 20$, there is relatively little variation in the ratios. Asymptotic values $P^{\widetilde{E''}}/D^{\widetilde{E''}} \approx 2.2$, $P^{\overline{\epsilon'}}/D^{\overline{\epsilon'}} \approx 1.1$, $P^{\widetilde{m_1''^2}}/D^{\widetilde{m_1''^2}} \approx 1.25$, and $P^{\widetilde{\chi''}}/D^{\widetilde{\chi''}} \approx 1$ were obtained; $P^{\widetilde{E''}}/D^{\widetilde{E''}}$ attains a larger value than in shear-driven flows. The production-to-dissipation/destruction ratios (profiles and integrated values) provide time-dependent constraints on the predictions of closures: constant ratios are necessary but insufficient for self-similarity. As discussed elsewhere,[1] the present DNS study focused on transitional Rayleigh–Taylor flow that reaches an early self-similar state at the latest time. A comparison of profiles of the terms in the budgets of the mean and turbulence equations considered here at the four times shown indicates that, generally, these profiles exhibit the most change in their magnitude between early times $t/t_c = 5.13$ and as the flow transitions to a more three-dimensional state at $t/t_c = 25.1$. There is significantly less change in the qualitative structure of the profiles between $t/t_c = 25.1$ and the latest time 37.9 representative of a weakly-turbulent, early self-similar state.

The results of this study are useful for examining and interpreting the detailed predictions of RANS or LES models of turbulent transport and mixing in transitional Rayleigh–Taylor instability-generated flow. The DNS data considered here considerably augments measurements from the water channel experiment. While the flow considered here satisfies the Boussinesq approximation, the budgets and the evolution of the terms may change for larger Atwood and Reynolds number flows, in which non-Boussinesq effects are manifested.

Acknowledgments

This work was performed under the auspices of the U.S. Department of Energy by Lawrence Livermore National Laboratory under Contract DE-AC52-07NA27344.

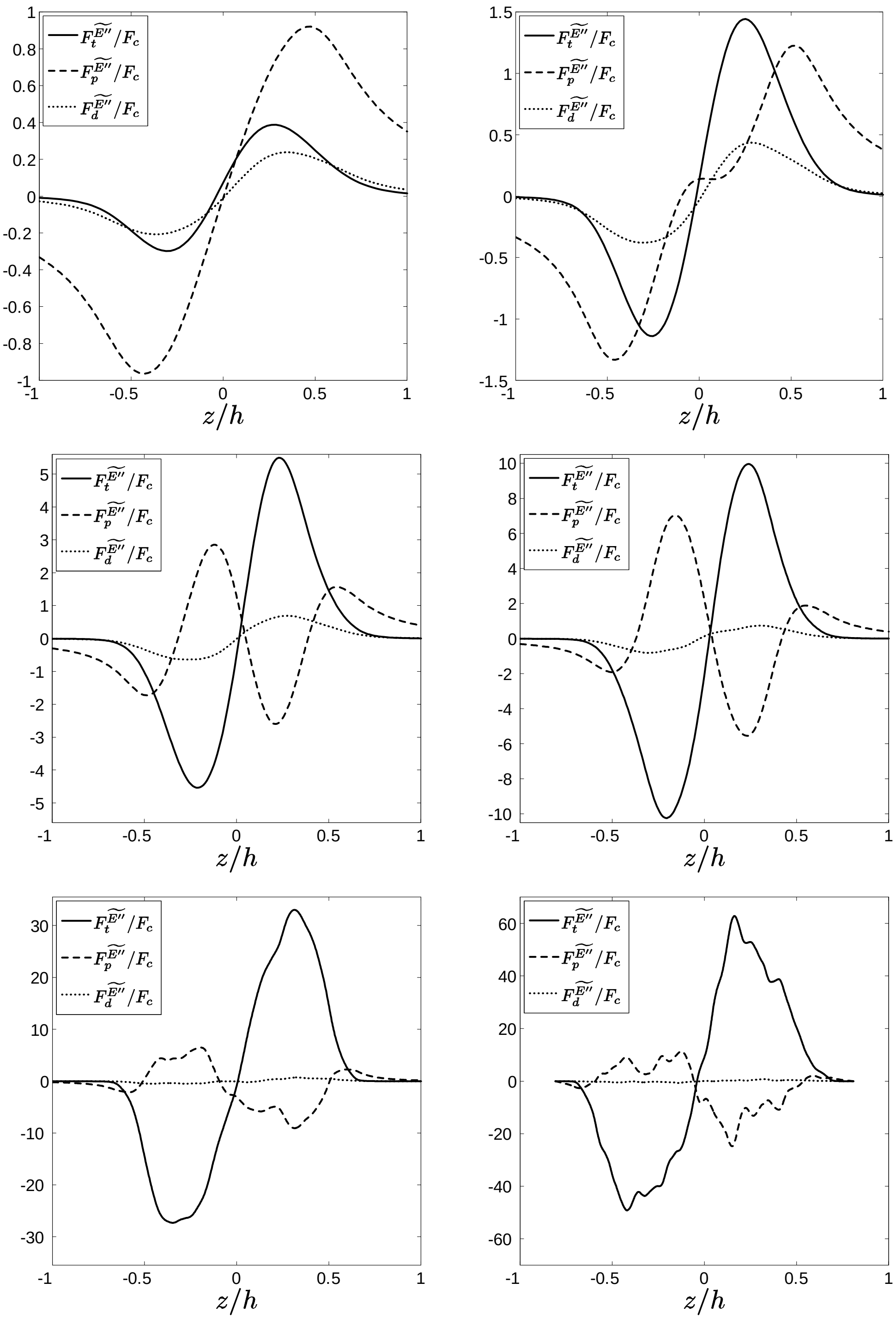

FIG. 18: Profiles of the fluxes normalized by $F_c = \rho_c u_c^3$ in the total turbulent kinetic energy transport $T^{\widetilde{E''}}$ at $t/t_c = 5.13$ (top left), 7.18 (top right), 10.1 (middle left), 12.6 (middle right), 25.1 (bottom left), and 37.9 (bottom right).

APPENDIX A: TURBULENT FLUXES

a. *Dynamics of turbulent, pressure, and viscous turbulent kinetic energy transport*

The total turbulent kinetic energy flux can be decomposed into its turbulent, pressure, and viscous components $F_t^{\widetilde{E''}} = \overline{\rho}\widetilde{E''w''}$, $F_p^{\widetilde{E''}} = \overline{p'w''}$, and $F_d^{\widetilde{E''}} = -\overline{\sigma_{i3}u_i''}$, respectively. These fluxes are examined in detail in Fig. 18 as canonical closure phenomenology neglects $F_d^{\widetilde{E''}}$ and combines $F_t^{\widetilde{E''}} + F_p^{\widetilde{E''}}$ into a single gradient-diffusion closure,[19] which is not entirely accurate for Rayleigh–

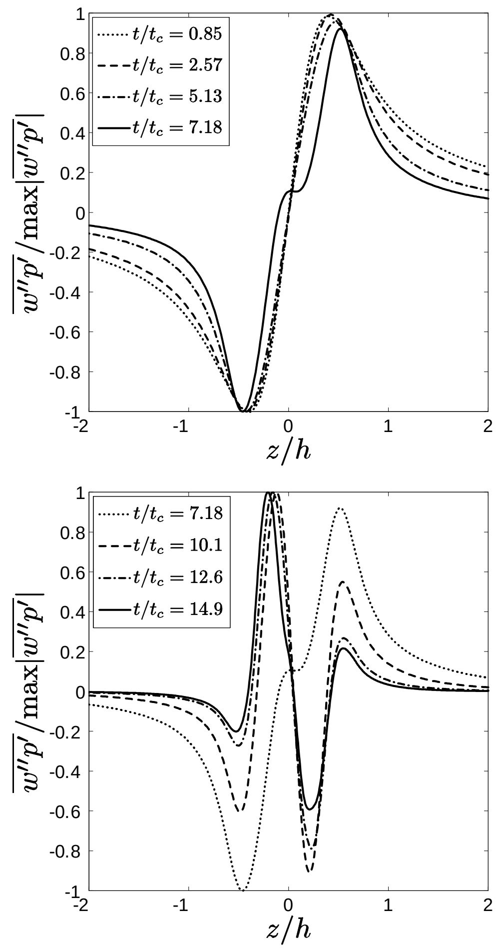

FIG. 19: Profiles of the pressure flux at early times (top) and intermediate times (bottom) normalized by its maximum value. The change of sign of $\overline{p'w''}$ within the core of the mixing layer occurs at $t/t_c = 7.19$.

Taylor mixing. All early-time fluxes indicate transfer of energy away from the center plane of the layer and toward its edges. The turbulent flux $F_t^{\widetilde{E''}}$ is least important for $t/t_c \leq 7.18$, so that gradient-diffusion models are not expected to capture the transport accurately at early times. The pressure transport has a significant, non-zero flux beyond the mixing layer boundaries. While the fluid outside the layer remains nearly inviscid, velocity fluctuations outside the layer exist due to the nonlocal pressure fluctuations created by rising and falling structures. This is the same process in which irrotational velocity fluctuations are induced by pressure fluctuations at the free stream edges of shear layers and jets.[41]

For $t/t_c \geq 7.18$, $F_t^{\widetilde{E''}}$ becomes the dominant flux, transferring turbulent kinetic energy away from the central core. The viscous flux is negligible; however, the pressure flux $F_p^{\widetilde{E''}}$ is not and exhibits more complex behavior. Within the mixing layer $|z/h| \leq 0.5$, $F_p^{\widetilde{E''}}$ opposes the turbulent kinetic energy flux in a counter-gradient manner. Outside the mixing layer ($|z/h| > 0.5$), the pressure flux re-aligns with the down-gradient flux of $\widetilde{E''}$. The pressure flux is the only significant mechanism for transport of velocity fluctuations outside the layer.

The pressure flux $F_p^{\widetilde{E''}}$ normalized by its maximum value at each time is shown in Fig. 19. The early-time bifurcation is seen as $F_p^{\widetilde{E''}}$ transports energy away from the mixing layer core for $t/t_c < 7.19$ and abruptly reverses sign to oppose $F_t^{\widetilde{E''}}$ for $t/t_c > 7.19$. This bifurcation corresponds to the initial formation of secondary vortices in-between rising and falling structures. As a result, low pressure pockets form in the centers of the vortices. Figure 3.49 in Ref. 7 shows the early-time evolution of a slice of the density and pressure fields, where the formation of secondary instabilities is apparent. This transition at $t/t_c = 7.19$ does not affect the behavior of $F_p^{\widetilde{E''}}$ beyond the layer edges ($|z/h| \geq 0.5$), where $F_p^{\widetilde{E''}}$ continues to remove energy, inducing velocity fluctuations in the quiescent pure fluid above and below the layer. This behavior of the pressure transport complicates the formulation of closure models of $T^{\widetilde{E''}}$ in Rayleigh–Taylor flow.

b. Dynamics of turbulent, pressure, and viscous turbulent kinetic energy dissipation rate transport

The total turbulent kinetic energy dissipation rate flux can be decomposed into its turbulent, pressure and viscous components $F_t^{\overline{\epsilon'}} = \overline{\rho}\overline{\epsilon' w'}$, $F_p^{\overline{\epsilon'}} = 2\overline{\nu}\overline{\frac{\partial p'}{\partial x_m}\frac{\partial w'}{\partial x_m}}$, and $F_d^{\overline{\epsilon'}} = -\overline{\mu}\partial\overline{\epsilon'}/\partial z$, respectively, which are shown in Fig. 20. The viscous flux is non-negligible at early-times. At small Reynolds numbers, the turbulent flux is either negligible or is of the same order as the other fluxes. The pressure flux at early times augments the turbulent flux, transporting $\overline{\epsilon'}$ away from the center plane. Applying standard $\widetilde{E''}$-$\overline{\epsilon'}$ models to small- and moderate-Reynolds number Rayleigh–Taylor mixing is complicated by this behavior.

The turbulent flux later becomes the dominant contribution to $T^{\overline{\epsilon'}}$ (see Fig. 20). A similar bifurcation is seen in the pressure flux $F_p^{\overline{\epsilon'}}$ as in $F_p^{\widetilde{E''}}$ (see Fig. 19), where the pressure transport of $\overline{\epsilon'}$ opposes the down-gradient flux of $\overline{\epsilon'}$. However, while similar behavior in $F_p^{\overline{\epsilon'}}$ is observed, the relative contribution of this term to $T^{\overline{\epsilon'}}$ is smaller than that of $F_p^{\widetilde{E''}}$ to $T^{\widetilde{E''}}$. In addition, the transport of $\overline{\epsilon'}$ to the irrotational fluid outside of the mixing layer (as seen in $F_p^{\widetilde{E''}}$) is not observed.

APPENDIX B: ORDER OF MAGNITUDE ESTIMATES OF TERMS IN THE TRANSPORT EQUATIONS

Using order of magnitude estimates similar to those for turbulent transport equations describing canonical

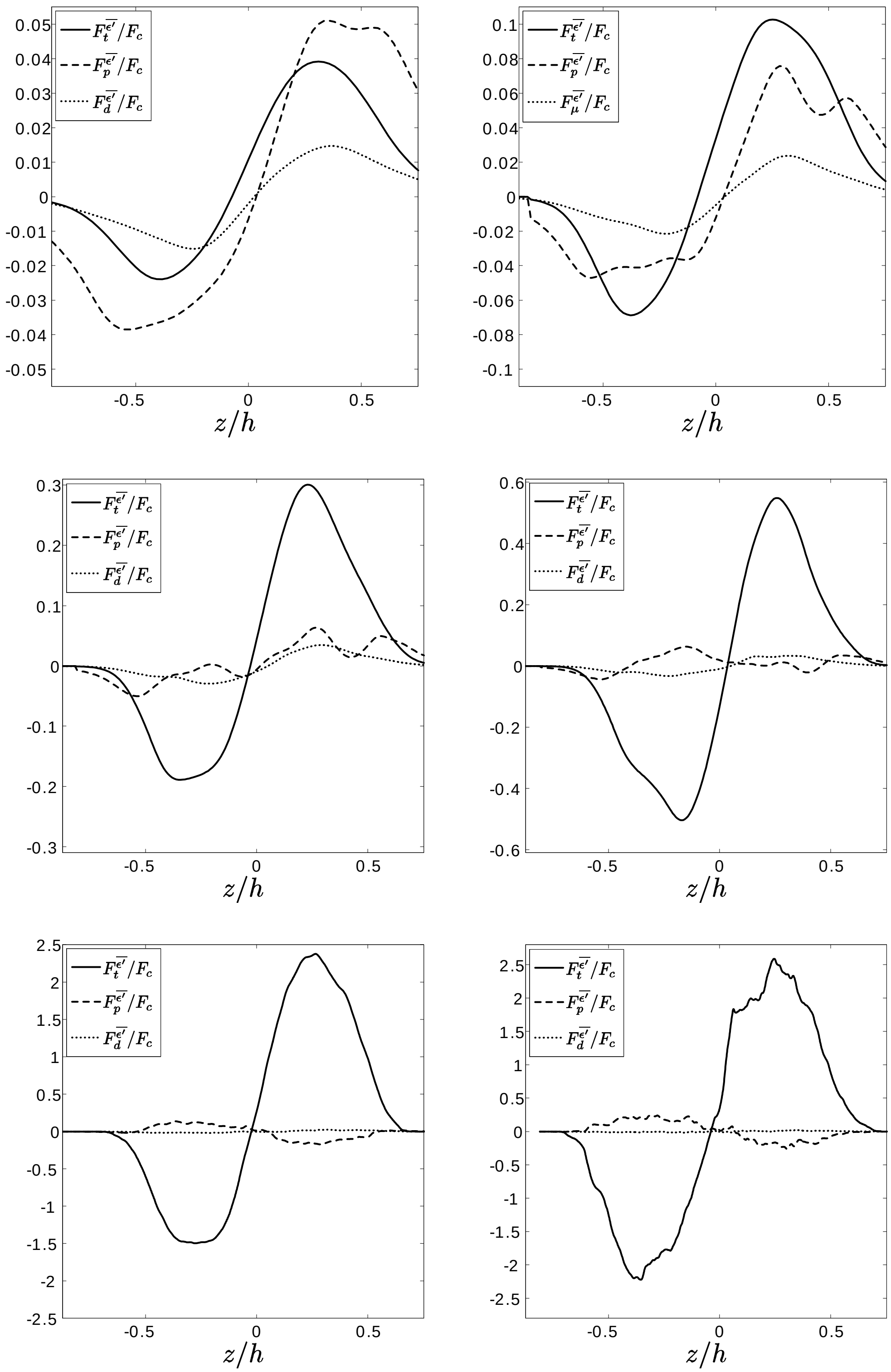

FIG. 20: Profiles of the fluxes normalized by $F_c = \rho_c u_c^3/t_c$ in the total turbulent kinetic energy dissipation rate transport $T^{\overline{\epsilon'}}$ at $t/t_c = 5.13$ top left), 7.18 (top right), 10.1 (middle left), 12.6 (middle right), 25.1 (bottom left), and 37.9 (bottom right).

incompressible flows,[29,42] it is possible to obtain additional insight into the expected dominance of terms in Rayleigh–Taylor flow by estimating their magnitude. For Rayleigh–Taylor flow, estimate the characteristic turbulent velocity and lengthscales by $u_h \sim u_{rms} \sim dh/dt$ and h, respectively, the characteristic density by $\overline{\rho} \sim \rho_0$, $\partial\overline{p}/\partial z = -\overline{\rho} g$, $p' \sim \rho_{rms} u_h^2$, and the fluctuating velocity divergence $\partial u_i''/\partial x_i \sim (\rho_{rms}/\rho_0)\, u_h/\lambda$, where $\lambda = \sqrt{15\overline{\nu}\widetilde{E''}/\overline{\epsilon'}}$ is the Taylor microscale. Noting that the vertical Reynolds stress can be interpreted as a 'turbulent pressure', $\tau_{33} = \overline{\rho}\widetilde{w''^2} \sim \rho_0 g h$; also, $\overline{w''} \sim -\overline{\rho' w'}/\overline{\rho} \sim \rho_{rms} u_h/\rho_0$. The mean velocity is $\widetilde{w} \sim \Delta\widetilde{w} \sim \overline{w} \sim \Delta\overline{w} \sim 0$. It follows that $\widetilde{E''} \sim u_h^2/2$, $\overline{\epsilon'} \sim \overline{\nu} u_h^2/\lambda^2 \sim u_h^3/(2h)$, and $\widetilde{\chi''} \sim \overline{D} m_{rms}^2/\lambda_m^2$, where $\lambda_m = \sqrt{12\overline{D}/\widetilde{\chi''}}\, m_{rms}$ is the heavy-fluid mass fraction Taylor microscale. With the definitions of the Reynolds numbers $\mathrm{Re}_h = h u_h/\overline{\nu}$, $\mathrm{Re}_\lambda = \lambda u_h/\overline{\nu}$, and $\mathrm{Re}_t = \left(\widetilde{E''}\right)^2/(\overline{\epsilon'}\,\overline{\nu})$, and $\lambda/h = \sqrt{15/\mathrm{Re}_h}$, it follows that $\mathrm{Re}_h = (h/\lambda)\mathrm{Re}_\lambda \sim 2\mathrm{Re}_t$ or $\mathrm{Re}_\lambda \sim \sqrt{15\mathrm{Re}_h} \sim \sqrt{30\mathrm{Re}_t}$. Applying these estimates to Eqs. (5), (7), (30), (31), (32), and (33) gives

$$\underbrace{\frac{\partial}{\partial t}(\overline{\rho}\,\widetilde{w})}_{\mathcal{O}\left(\frac{\rho_0\,\widetilde{w}\,u_h}{h}\right)} + \underbrace{\frac{\partial}{\partial z}(\overline{\rho}\,\widetilde{w}^2)}_{\mathcal{O}\left(\frac{\rho_0\,\widetilde{w}^2\,u_h}{h}\right)} = -\underbrace{\overline{\rho}\,g}_{\mathcal{O}(\rho_0\,g)} \underbrace{-\frac{\partial\overline{p}}{\partial z}}_{\mathcal{O}(\rho_0\,g)} + \underbrace{\frac{\partial\overline{\sigma}_{33}}{\partial z}}_{\mathcal{O}\left(\frac{\overline{\mu}\,\widetilde{w}}{h^2}\right)} - \underbrace{\frac{\partial\tau_{33}}{\partial z}}_{\mathcal{O}(\rho_0\,g)}\,, \tag{B1}$$

$$\underbrace{\frac{\partial}{\partial t}(\overline{\rho}\,\widetilde{m}_1)}_{\mathcal{O}\left(\frac{\rho_0\,m_0\,u_h}{h}\right)} + \underbrace{\frac{\partial}{\partial z}(\overline{\rho}\,\widetilde{m}_1\,\widetilde{w})}_{\mathcal{O}\left(\frac{\rho_0\,m_0\,\widetilde{w}}{h}\right)} = -\underbrace{\frac{\partial}{\partial z}\left(\overline{\rho}\,\widetilde{m_1''\,w''}\right)}_{\mathcal{O}\left(\frac{\rho_0\,m_{rms}\,u_h}{h}\right)} + \underbrace{\frac{\partial}{\partial z}\left(\frac{\overline{\mu}}{Sc}\,\frac{\partial\widetilde{m}_1}{\partial z}\right)}_{\mathcal{O}\left(\frac{\rho_0\,D\,\Delta m}{h^2}\right)}, \tag{B2}$$

$$\begin{aligned} \underbrace{\frac{\partial}{\partial t}\left(\overline{\rho}\,\widetilde{E''}\right)}_{\mathcal{O}\left(\frac{\rho_0\,u_h^3}{2\,h}\right)} + \underbrace{\frac{\partial}{\partial z}\left(\overline{\rho}\,\widetilde{E''}\,\widetilde{w}\right)}_{\mathcal{O}\left(\frac{\rho_0\,u_h^2\,\widetilde{w}}{2\,h}\right)} = {} & \underbrace{-\overline{w''}\,\frac{\partial\overline{p}}{\partial z}}_{\mathcal{O}(\rho_{rms}\,g\,u_h)} - \underbrace{\tau_{33}\,\frac{\partial\widetilde{w}}{\partial z}}_{\mathcal{O}(\rho_0\,g\,\Delta\widetilde{w})} + \underbrace{\overline{p'\,\frac{\partial u_i''}{\partial x_i}}}_{\mathcal{O}\left(\frac{\rho_{rms}\,u_h^3}{\lambda}\right)} - \underbrace{\overline{\rho}\,\widetilde{\epsilon''}}_{\mathcal{O}\left(\frac{\overline{\mu}\,u_h^2}{\lambda^2}\right)} \\ & -\underbrace{\frac{\partial}{\partial z}\left(\overline{\rho}\,\widetilde{E''\,w''}\right)}_{\mathcal{O}\left(\frac{\rho_0\,u_h^3}{2\,h}\right)} - \underbrace{\frac{\partial}{\partial z}\left(\overline{p'\,w''}\right)}_{\mathcal{O}\left(\frac{\rho_{rms}\,u_h^3}{h}\right)} + \underbrace{\frac{\partial}{\partial z}\left(\overline{\sigma_{33}\,w''}\right)}_{\mathcal{O}\left(\frac{\overline{\mu}\,u_h^2}{\lambda\,h}\right)}, \end{aligned} \tag{B3}$$

$$\begin{aligned} \underbrace{\frac{\partial}{\partial t}(\overline{\rho}\,\overline{\epsilon'})}_{\mathcal{O}\left(\frac{\rho_0\,u_h^4}{2\,h^2}\right)} + \underbrace{\frac{\partial}{\partial z}(\overline{\rho}\,\overline{\epsilon'}\,\overline{w})}_{\mathcal{O}\left(\frac{\rho_0\,u_h^3\,\overline{w}}{2\,h^2}\right)} = {} & \underbrace{-2\,\overline{\nu}\,g\,\overline{\frac{\partial\rho'}{\partial x_j}\,\frac{\partial w'}{\partial x_j}}}_{\mathcal{O}\left(\frac{2\,\overline{\nu}\,g\,\rho_{rms}\,u_h}{\lambda^2}\right)} \underbrace{-2\,\overline{\mu}\,\overline{\frac{\partial u_i'}{\partial x_k}\,\frac{\partial u_i'}{\partial x_j}\,\frac{\partial u_k'}{\partial x_j}}}_{\mathcal{O}\left(\frac{2\,\overline{\mu}\,u_h^3}{\lambda^3}\right)} \\ & \underbrace{-2\,\overline{\mu}\left(\overline{\frac{\partial w'}{\partial x_k}\,\frac{\partial w'}{\partial x_k}} + \overline{\frac{\partial u_k'}{\partial z}\,\frac{\partial u_k'}{\partial z}}\right)\frac{\partial\overline{w}}{\partial z}}_{\mathcal{O}\left(\frac{4\,\overline{\mu}\,u_h^2\,\Delta\overline{w}}{\lambda^2\,h}\right)} - \underbrace{\overline{\mu}\,\overline{w'\,\frac{\partial w'}{\partial z}}\,\frac{\partial^2\overline{w}}{\partial z^2}}_{\mathcal{O}\left(\frac{\overline{\mu}\,u_h^2\,\Delta\overline{w}}{\lambda\,h^2}\right)} \underbrace{-2\,\overline{\mu}\,\overline{\nu}\,\overline{\left(\frac{\partial^2 u_i'}{\partial x_j\partial x_k}\right)^2}}_{\mathcal{O}\left(\frac{2\,\overline{\mu}\,\overline{\nu}\,u_h^2}{\lambda^2\,\delta^2}\right)} \\ & -\underbrace{\frac{\partial}{\partial z}(\overline{\rho}\,\overline{\epsilon'\,w'})}_{\mathcal{O}\left(\frac{\rho_0\,u_h^4}{2\,h^2}\right)} - \underbrace{\frac{\partial}{\partial z}\left(2\,\overline{\nu}\,\overline{\frac{\partial p'}{\partial x_k}\,\frac{\partial w'}{\partial x_k}}\right)}_{\mathcal{O}\left(\frac{2\,\overline{\nu}\,\rho_{rms}\,u_h^3}{\lambda^2\,h}\right)} + \underbrace{\frac{\partial}{\partial z}\left(\overline{\mu}\,\frac{\partial\overline{\epsilon'}}{\partial z}\right)}_{\mathcal{O}\left(\frac{\overline{\mu}\,u_h^3}{2\,h^3}\right)}, \end{aligned} \tag{B4}$$

$$\underbrace{\frac{\partial}{\partial t}\left(\overline{\rho}\,\widetilde{m_1''^2}\right)}_{\mathcal{O}\left(\frac{\rho_0\,m_{rms}^2\,u_h}{\lambda_m}\right)} + \underbrace{\frac{\partial}{\partial z}\left(\overline{\rho}\,\widetilde{m_1''^2}\,\widetilde{w}\right)}_{\mathcal{O}\left(\frac{\rho_0\,m_{rms}^2\,\widetilde{w}}{h}\right)} = \underbrace{-2\,\overline{\rho}\,\widetilde{m_1''\,w''}\,\frac{\partial \widetilde{m}_1}{\partial z}}_{\mathcal{O}\left(\frac{2\,\rho_0\,u_h\,m_{rms}\,\Delta m}{h}\right)} - \underbrace{2\,\overline{\rho}\,\widetilde{\chi''}}_{\mathcal{O}\left(\frac{2\,\overline{D}\,\rho_0\,m_{rms}^2}{\lambda_m^2}\right)} - \underbrace{\frac{\partial}{\partial z}\left(\overline{\rho}\,\widetilde{m_1''^2\,w''}\right)}_{\mathcal{O}\left(\frac{\rho_0\,m_{rms}^2\,u_h}{h}\right)} + \underbrace{\frac{\partial}{\partial z}\left(\overline{\rho}\,\overline{D}\,\frac{\partial \widetilde{m_1''^2}}{\partial z}\right)}_{\mathcal{O}\left(\frac{\overline{D}\,\rho_0\,m_{rms}^2}{h^2}\right)}, \tag{B5}$$

$$\underbrace{\frac{\partial}{\partial t}\left(\overline{\rho}\,\widetilde{\chi''}\right)}_{\mathcal{O}\left(\frac{\overline{D}\,\rho_0\,m_{rms}^2\,u_h}{\lambda_m^3}\right)} + \underbrace{\frac{\partial}{\partial z}\left(\overline{\rho}\,\widetilde{\chi''}\,\widetilde{w}\right)}_{\mathcal{O}\left(\frac{\overline{D}\,\rho_0\,m_{rms}^2\,\widetilde{w}}{\lambda_m^2\,h}\right)} = \underbrace{-2\,\overline{D}\,\overline{\rho\,\frac{\partial m_1''}{\partial x_j}\,\frac{\partial w''}{\partial x_j}}\,\frac{\partial \widetilde{m}_1}{\partial z}}_{\mathcal{O}\left(\frac{2\,\overline{D}\,\rho_0\,m_{rms}\,\Delta m\,u_h}{h\,\lambda_m\,\lambda}\right)} \underbrace{-2\,\overline{D}\,\overline{\rho\,\frac{\partial m_1''}{\partial x_i}\,\frac{\partial m_1''}{\partial x_j}\,\frac{\partial u_j''}{\partial x_i}}}_{\mathcal{O}\left(\frac{2\,\overline{D}\,\rho_0\,m_{rms}^2\,u_h}{\lambda_m^2\,\lambda}\right)}$$
$$\underbrace{-2\,\overline{D}\,\overline{\rho\,\frac{\partial m_1''}{\partial z}\,\frac{\partial m_1''}{\partial z}}\,\frac{\partial \widetilde{w}}{\partial z}}_{\mathcal{O}\left(\frac{2\,\overline{D}\,\rho_0\,m_{rms}^2\,\Delta\widetilde{w}}{h\,\lambda_m^2}\right)} \underbrace{-2\,\overline{D}\,\overline{\rho\,w''\,\frac{\partial m_1''}{\partial z}}\,\frac{\partial^2 \widetilde{m}_1}{\partial z^2}}_{\mathcal{O}\left(\frac{2\,\overline{D}\,\rho_0\,m_{rms}\,\Delta m\,u_h}{h^2\,\lambda_m}\right)} - \underbrace{2\,\overline{D}^2\,\overline{\rho\left(\frac{\partial^2 m_1''}{\partial x_i \partial x_j}\right)^2}}_{\mathcal{O}\left(\frac{2\,\overline{D}^2\,\rho_0\,m_{rms}^2}{\lambda_m^2\,\delta_m^2}\right)}$$
$$- \underbrace{\frac{\partial}{\partial z}\left(\overline{\rho}\,\widetilde{\chi''\,w''}\right)}_{\mathcal{O}\left(\frac{\rho_0\,\overline{D}\,m_{rms}^2\,u_h}{h\,\lambda_m^2}\right)} + \underbrace{\frac{\partial}{\partial z}\left(\overline{\rho}\,\overline{D}\,\frac{\partial \widetilde{\chi''}}{\partial z}\right)}_{\mathcal{O}\left(\frac{\rho_0\,\overline{D}^2\,m_{rms}^2}{h^2\,\lambda_m^2}\right)}, \tag{B6}$$

where δ and δ_m are additional lengthscales associated with dissipation of turbulent kinetic energy and heavy-fluid mass fraction variance, respectively. The lengthscales appropriate for the dissipation term imply a combination of λ and δ, where δ is determined by requiring $P_t^{\widetilde{\epsilon'}} \approx D^{\widetilde{\epsilon'}}$,[29] i.e., $\delta = \lambda/\sqrt{\mathrm{Re}_\lambda}$. Similarly, δ_m is determined by requiring $P_t^{\widetilde{\chi''}} \approx D^{\widetilde{\chi''}}$, i.e., $\delta_m = \lambda/\sqrt{\mathrm{Re}_\lambda \mathrm{Sc}}$. It follows that $\lambda/\lambda_m = \sqrt{5\mathrm{Sc}\,\widetilde{E''}\widetilde{\chi''}/\left(4\widetilde{\epsilon'}m_{rms}^2\right)} \approx \sqrt{5\mathrm{Sc}/4}$, as the mechanical-to-scalar timescale ratio $R \propto \widetilde{E''}\widetilde{\chi''}/\left(\widetilde{\epsilon'}m_{rms}^2\right) \sim$ *constant*. The order of magnitude of the terms in the $\widetilde{\chi''}$ equation were also considered in nonreacting and reacting flow.[33]

In the estimates of terms in the mean and turbulent transport equations, the order of magnitude estimates above together with the following estimates from the DNS will be used. At the latest time in the simulation ($t/t_c = 37.9$), $t = \sqrt{H/(gA)}\tau \sim 6.6\tau \sim 10$ s, at which time $h \sim 15$ cm, $u_h \sim 1.8$ cm/s (see Fig. 8 of Ref. 1), and $\mathrm{Re}_h \sim 2666$. The late-time self-similar scalings $h \sim \alpha A g t^2$ and $u_h \sim 2\alpha A g t$ *cannot be used*, as h also depends on a constant and linear term.[13] Using Eq. (23) of Ref. 1 and the late-time estimate $m_{rms} = \sqrt{\widetilde{m_1''^2}} \sim 0.05$ from Fig. 15, it follows that $\rho_{rms} \sim \Delta\rho\sqrt{m_{rms}} \sim 3.47\times10^{-4}$ g/cm^3 and $\rho_0 \sim (\rho_1+\rho_2)/2 \sim 1$ g/cm^3. With $m_0 \sim 0.5$, $m_{rms}/m_0 \sim 0.1$. Furthermore, $h/\lambda \sim 13.33$ (or $\lambda \sim 1.125$ cm) and $\lambda_m \sim \lambda/3 \sim 0.375$ cm.

APPENDIX C: DERIVATION OF THE EXACT TURBULENCE EQUATIONS FOR SMALL ATWOOD NUMBER RAYLEIGH–TAYLOR FLOW

The exact unclosed turbulence equations are derived here for a variable-density flow described by Eqs. (1a)–(1c). Exhibiting these equations is also helpful in determining which terms have been explicitly modeled and neglected in previously proposed RANS models of Rayleigh–Taylor instability-induced turbulent flow.

1. The exact turbulent kinetic energy transport equation

To derive the exact turbulent kinetic energy transport equation, first form the fluctuating Navier–Stokes equation by introducing the Favre–Reynolds decompositions $u_i = \widetilde{u}_i + u_i''$ and $p = \overline{p} + p'$ into Eq. (1b) and substituting $\partial\widetilde{u}_i/\partial t$

from Eq. (5):

$$\rho\left(\frac{\partial}{\partial t}+\widetilde{u}_j\,\frac{\partial}{\partial x_j}\right)u_i'' = -\rho\,u_j''\,\frac{\partial\widetilde{u}_i}{\partial x_j} - \rho\,u_j''\,\frac{\partial u_i''}{\partial x_j} + \frac{\partial}{\partial x_j}(\sigma_{ij}-\overline{p}\,\delta_{ij}-p'\,\delta_{ij}) - \frac{\rho}{\overline{\rho}}\,\frac{\partial}{\partial x_j}(\overline{\sigma}_{ij}-\overline{p}\,\delta_{ij}-\tau_{ij})\,. \tag{C1}$$

Note that the body force has vanished. Multiplying Eq. (C1) by u_i'' and ensemble averaging gives (using $\overline{\rho u_i''}=0$ and the mean continuity equation)

$$\begin{aligned}\overline{\rho}\left(\frac{\partial}{\partial t}+\widetilde{u}_j\,\frac{\partial}{\partial x_j}\right)\frac{\widetilde{u''^2}}{2} \;=\;& \overline{\frac{u''^2}{2}\left[\frac{\partial\rho}{\partial t}+\frac{\partial}{\partial x_j}(\rho\,\widetilde{u}_j)\right]} - \overline{\rho\,u_i''\,u_j''}\,\frac{\partial\widetilde{u}_i}{\partial x_j} - \overline{\rho\,u_i''\,u_j''\,\frac{\partial u_i''}{\partial x_j}} \\ & +\overline{u_i''\,\frac{\partial}{\partial x_j}(\sigma_{ij}-\overline{p}\,\delta_{ij})} - \overline{u_i''\,\frac{\partial p'}{\partial x_i}}\,.\end{aligned} \tag{C2}$$

Using homogeneity in the xy-plane (so that spatial derivatives and averaging commute), and the identities

$$\begin{aligned}\overline{\frac{u''^2}{2}\left[\frac{\partial\rho}{\partial t}+\frac{\partial}{\partial x_j}(\rho\,\widetilde{u}_j)\right]} - \overline{\rho\,u_i''\,u_j''\,\frac{\partial u_i''}{\partial x_j}} &= \overline{\frac{u''^2}{2}\left[\frac{\partial\rho}{\partial t}+\frac{\partial}{\partial x_j}(\rho\,\widetilde{u}_j)\right]} - \overline{\rho\,u_j''\,\frac{\partial}{\partial x_j}\left(\frac{u''^2}{2}\right)} \\ &= \overline{\frac{u''^2}{2}\left[\frac{\partial\rho}{\partial t}+\frac{\partial}{\partial x_j}(\rho\,\widetilde{u}_j)\right]} - \frac{\partial}{\partial x_j}\left(\frac{\overline{\rho\,u''^2\,u_j''}}{2}\right) + \overline{\frac{u''^2}{2}\,\frac{\partial}{\partial x_j}(\rho\,u_j'')} \\ &= -\frac{\partial}{\partial x_j}\left(\frac{\overline{\rho\,u''^2\,u_j''}}{2}\right),\end{aligned}$$

$$\overline{u_i''\,\frac{\partial}{\partial x_j}(\sigma_{ij}-p'\,\delta_{ij})} = \frac{\partial}{\partial x_j}\left(\overline{\sigma_{ij}\,u_i''-p'\,u_j''}\right) - \overline{\sigma_{ij}\,\frac{\partial u_i''}{\partial x_j}} + \overline{p'\,\frac{\partial u_j''}{\partial x_j}}$$

to rewrite terms in Eq. (C2) gives Eq. (14).

2. The exact turbulent kinetic energy dissipation transport equation

To derive the exact incompressible turbulent kinetic energy dissipation rate transport equation, first substitute $u_i=\overline{u}_i+u_i'$, $\rho=\overline{\rho}+\rho'$, and $p=\overline{p}+p'$ into Eq. (1b) and subtract the Reynolds-averaged incompressible Navier–Stokes equation

$$\frac{\partial}{\partial t}(\rho\,\overline{u}_i)+\frac{\partial}{\partial x_j}(\rho\,\overline{u}_i\,\overline{u}_j) = \rho\left(\frac{\partial}{\partial t}+\overline{u}_j\,\frac{\partial}{\partial x_j}\right)\overline{u}_i = \overline{\rho}\,g_i - \frac{\partial\overline{p}}{\partial x_i} - \frac{\partial\tau_{ij}}{\partial x_j} + \overline{\mu}\,\nabla^2\overline{u}_i\,, \tag{C3}$$

from the resulting equation to obtain the fluctuating velocity evolution equation

$$\begin{aligned}\rho\,\frac{\partial u_i'}{\partial t}+\rho\,\frac{\partial}{\partial x_j}\left(\overline{u}_i\,u_j'+u_i'\,\overline{u}_j+u_i'\,u_j'\right) \;&=\; \rho\left(\frac{\partial}{\partial t}+\overline{u}_j\,\frac{\partial}{\partial x_j}\right)u_i' + \rho\,u_j'\,\frac{\partial\overline{u}_i}{\partial x_j} + \rho\,\frac{\partial}{\partial x_j}\left(u_i'\,u_j'\right) \\ &=\; \rho'\,g_i - \frac{\partial p'}{\partial x^i} + \frac{\partial\tau_{ij}}{\partial x_j} + \overline{\mu}\,\nabla^2 u_i'\,.\end{aligned} \tag{C4}$$

Using $\overline{\rho}\overline{\epsilon'}=\overline{\mu}\overline{(\partial v_i'/\partial x_j)^2}$ it follows that (assuming that $\mathbf{g}$ is independent of $\mathbf{x}$)

$$\begin{aligned}\frac{\partial\overline{\epsilon'}}{\partial t} \;&=\; 2\,\overline{\nu}\,\overline{\frac{\partial u_i'}{\partial x_j}\,\frac{\partial}{\partial x_j}\left(\frac{\partial u_i'}{\partial t}\right)} \\ &=\; 2\,\overline{\nu}\,\overline{\frac{\partial u_i'}{\partial x_j}\,\frac{\partial}{\partial x_j}\left[\frac{\rho'\,g_i}{\rho} - \frac{1}{\rho}\,\frac{\partial p'}{\partial x^i} + \frac{1}{\rho}\,\frac{\partial\tau_{ik}}{\partial x_k} + \overline{\nu}\,\nabla^2 u_i' - u_k'\,\frac{\partial\overline{u}_i}{\partial x_k} - \overline{u}_k\,\frac{\partial u_i'}{\partial x_k} - \frac{\partial}{\partial x_k}(u_i'\,u_k')\right]} \\ &=\; \frac{2\,\overline{\nu}}{\rho}\,g_i\,\overline{\frac{\partial\rho'}{\partial x_j}\,\frac{\partial u_i'}{\partial x_j}} - \frac{2\,\overline{\nu}}{\rho}\,\overline{\frac{\partial^2 p'}{\partial x_i\partial x_j}\,\frac{\partial u_i'}{\partial x_j}} + 2\,\overline{\nu}^2\,\overline{\frac{\partial u_i'}{\partial x_j}\,\nabla^2\left(\frac{\partial u_i'}{\partial x_j}\right)} - 2\,\overline{\nu}\,\overline{\frac{\partial u_i'}{\partial x_j}\,\frac{\partial u_k'}{\partial x_j}}\,\frac{\partial\overline{u}_i}{\partial x_k} \\ &\quad -2\,\overline{\nu}\,\overline{\frac{\partial u_i'}{\partial x_j}\,u_k'}\,\frac{\partial^2\overline{u}_i}{\partial x_j\partial x_k} - 2\,\overline{\nu}\,\overline{\frac{\partial u_i'}{\partial x_j}\,\frac{\partial u_i'}{\partial x_k}}\,\frac{\partial\overline{u}_k}{\partial x_j} - 2\,\overline{\nu}\,\overline{\frac{\partial u_i'}{\partial x_j}\,\frac{\partial^2 u_i'}{\partial x_j\partial x_k}}\,\overline{u}_k - 2\,\overline{\nu}\,\overline{\frac{\partial u_i'}{\partial x_j}\,\frac{\partial^2}{\partial x_j\partial x_k}(u_i'\,u_k')}\,.\end{aligned} \tag{C5}$$

Using the identities (where incompressibility $\partial\overline{u}_k/\partial x_k = \partial u'_k/\partial x_k = 0$ has been used)

$$\overline{\frac{\partial^2 p'}{\partial x_k \partial x_j}\,\frac{\partial u'_k}{\partial x_j}} = \frac{\partial}{\partial x_k}\left(\overline{\frac{\partial p'}{\partial x_j}\,\frac{\partial u'_k}{\partial x_j}}\right),$$

$$\overline{\frac{\partial u'_i}{\partial x_j}\,\nabla^2\left(\frac{\partial u'_i}{\partial x_j}\right)} = \frac{\partial}{\partial x_k}\left(\overline{\frac{\partial u'_i}{\partial x_j}\,\frac{\partial^2 u'_i}{\partial x_j \partial x_k}}\right) - \overline{\left(\frac{\partial^2 u'_i}{\partial x_j \partial x_k}\right)^2} = \frac{1}{2}\,\nabla^2\left[\overline{\left(\frac{\partial u'_i}{\partial x_j}\right)^2}\right] - \overline{\left(\frac{\partial^2 u'_i}{\partial x_j \partial x_k}\right)^2},$$

$$\overline{\frac{\partial u'_i}{\partial x_j}\,\frac{\partial u'_i}{\partial x_k}\,\frac{\partial \overline{u}_k}{\partial x_j}} = \overline{\frac{\partial u'_i}{\partial x_j}\,\frac{\partial u'_i}{\partial x_k}\,\frac{\partial \overline{u}_j}{\partial x_k}} = \overline{\frac{\partial u'_j}{\partial x_i}\,\frac{\partial u'_j}{\partial x_k}\,\frac{\partial \overline{u}_i}{\partial x_k}}\,,\quad \overline{\frac{\partial u'_i}{\partial x_j}\,\frac{\partial^2 u'_i}{\partial x_j \partial x_k}}\,\overline{u}_k = \frac{1}{2}\,\overline{u}_k\,\frac{\partial}{\partial x_k}\left[\overline{\left(\frac{\partial u'_i}{\partial x_j}\right)^2}\right],$$

$$\overline{\frac{\partial u'_i}{\partial x_j}\,\frac{\partial^2}{\partial x_j \partial x_k}(u'_i\,u'_k)} = \overline{\frac{\partial u'_i}{\partial x_j}\,\frac{\partial u'_i}{\partial x_k}\,\frac{\partial u'_k}{\partial x_j}} + \frac{1}{2}\,\frac{\partial}{\partial x_k}\left(\overline{u'_k\,\frac{\partial u'_i}{\partial x_j}\,\frac{\partial u'_i}{\partial x_j}}\right)$$

and rearranging terms gives Eq. (17) .

3. The exact heavy-fluid mass fraction variance transport equation

To derive the exact heavy-fluid mass fraction variance transport equation, assuming that $D = \overline{D} = \textit{constant}$, first form the fluctuating heavy-fluid mass fraction variance equation by introducing the decompositions $u_i = \widetilde{u}_i + u''_i$ and $m_1 = \widetilde{m}_1 + m''_1$ into Eq. (1c) and substituting $\partial\widetilde{m}_1/\partial t$ from Eq. (7):

$$\begin{aligned} \frac{\partial}{\partial t}(\rho\, m''_1) + \frac{\partial}{\partial x_j}(\rho\, m''_1\,\widetilde{u}_j) \;=\;& \frac{\partial}{\partial x_j}\left(\rho\, D\,\frac{\partial \widetilde{m}_1}{\partial x_j} + \rho\, D\,\frac{\partial m''_1}{\partial x_j}\right) - \frac{\partial}{\partial x_j}(\rho\, m''_1\, u''_j) \\ & -\rho\, u''_j\,\frac{\partial \widetilde{m}_1}{\partial x_j} + \frac{\rho}{\overline{\rho}}\,\frac{\partial}{\partial x_j}\left(\overline{\rho}\,\widetilde{m''_1\, u''_j} - \overline{\rho}\, D\,\frac{\partial \widetilde{m}_1}{\partial x_j}\right). \end{aligned} \tag{C6}$$

Multiplying by m''_1 and Reynolds averaging (using $\overline{\rho m''_1} = 0$) gives

$$\begin{aligned} \frac{\partial}{\partial t}\left(\frac{\overline{\rho\, m''^2_1}}{2}\right) + \frac{\partial}{\partial x_j}\left(\frac{\overline{\rho\, m''^2_1\,\widetilde{u}_j}}{2}\right) - \overline{\frac{m''^2_1}{2}\left[\frac{\partial \rho}{\partial t} + \frac{\partial}{\partial x_j}(\rho\,\widetilde{u}_j)\right]} \;=\;& \frac{\partial}{\partial x_j}\left[\overline{\rho\, m''_1\, D\,\frac{\partial \widetilde{m}_1}{\partial x^j} + \rho\, D\,\frac{\partial}{\partial x^j}\left(\frac{m''^2_1}{2}\right)}\right] \\ & -\overline{\rho\, D\left(\frac{\partial \widetilde{m}_1}{\partial x^j} + \frac{\partial m''_1}{\partial x^j}\right)\frac{\partial m''_1}{\partial x_j}} \\ & -\frac{\partial}{\partial x_j}\left(\frac{\overline{\rho\, m''^2_1\, u''_j}}{2}\right) + \overline{\frac{m''^2_1}{2}\,\frac{\partial}{\partial x_j}(\rho\, u''_j)} \\ & -\overline{\rho\, m''_1\, u''_j}\,\frac{\partial \widetilde{m}_1}{\partial x_j}\,. \end{aligned}$$

Using homogeneity and the identity

$$\overline{\frac{m''^2_1}{2}\left[\frac{\partial \rho}{\partial t} + \frac{\partial}{\partial x_j}(\rho\,\widetilde{u}_j)\right]} + \overline{\frac{m''^2_1}{2}\,\frac{\partial}{\partial x_j}(\rho\, u''_j)} = \overline{\frac{m''^2_1}{2}\left[\frac{\partial \rho}{\partial t} + \frac{\partial}{\partial x_j}(\rho\, u_j)\right]} = 0$$

gives Eq. (19).

4. The exact heavy-fluid mass fraction variance dissipation rate transport equation

To derive the exact heavy-fluid mass fraction variance dissipation rate transport equation, use Eq. (21), assuming that D is constant, and $\overline{\rho \partial m_1''/\partial x_j} = 0$:

$$\begin{aligned}
\frac{\partial}{\partial t}\left(\overline{\rho}\,\widetilde{\chi''}\right) &= 2\,\overline{D}\,\overline{\rho\,\frac{\partial m_1''}{\partial x_j}\,\frac{\partial}{\partial t}\left(\frac{\partial m_1''}{\partial x_j}\right)} + \overline{D}\,\overline{\frac{\partial \rho}{\partial t}\left(\frac{\partial m_1''}{\partial x_j}\right)^2} = 2\,\overline{D}\,\overline{\rho\,\frac{\partial m_1''}{\partial x_j}\,\frac{\partial}{\partial x_j}\left(\frac{\partial m_1''}{\partial t}\right)} - \overline{D}\,\overline{\left(\frac{\partial m_1''}{\partial x_j}\right)^2\frac{\partial}{\partial x_k}(\rho\,u_k)} \\
&= 2\,\overline{D}\,\overline{\rho\,\frac{\partial m_1''}{\partial x_j}\,\frac{\partial}{\partial x_j}\left[-\widetilde{u}_k\,\frac{\partial m_1''}{\partial x_k} - u_k''\,\frac{\partial \widetilde{m}_1}{\partial x_k} - u_k''\,\frac{\partial m_1''}{\partial x_k} + \frac{1}{\rho}\,\frac{\partial}{\partial x_k}\left(\rho\,\overline{D}\,\frac{\partial m_1}{\partial x_k}\right)\right]} \\
&\quad +2\,\overline{D}\,\overline{\rho\,\frac{\partial m_1''}{\partial x_j}\,\frac{\partial}{\partial x_j}\left[\frac{1}{\overline{\rho}}\,\frac{\partial}{\partial x_k}\left(\overline{\rho}\,\widetilde{m_1''\,u_k''} - \overline{\rho}\,\overline{D}\,\frac{\partial \widetilde{m}_1}{\partial x_k}\right)\right]} - \overline{D}\,\overline{\left(\frac{\partial m_1''}{\partial x_j}\right)^2\frac{\partial}{\partial x_k}(\rho\,u_k)} \\
&= -2\,\overline{D}\,\overline{\rho\,\frac{\partial m_1''}{\partial x_j}\left(\frac{\partial \widetilde{u}_k}{\partial x_j}\,\frac{\partial m_1''}{\partial x_k} + \widetilde{u}_k\,\frac{\partial^2 m_1''}{\partial x_j \partial x_k} + \frac{\partial u_k''}{\partial x_j}\,\frac{\partial \widetilde{m}_1}{\partial x_k} + u_k''\,\frac{\partial^2 \widetilde{m}_1}{\partial x_j \partial x_k}\right)} \\
&\quad -2\,\overline{D}\,\overline{\rho\,\frac{\partial m_1''}{\partial x_j}\left(\frac{\partial u_k''}{\partial x_j}\,\frac{\partial m_1''}{\partial x_k} + u_k''\,\frac{\partial^2 m_1''}{\partial x_j \partial x_k}\right)} + 2\,\overline{D}\,\overline{\rho\,\frac{\partial m_1''}{\partial x_j}\,\frac{\partial}{\partial x_j}\left[\frac{1}{\rho}\,\frac{\partial}{\partial x_k}\left(\rho\,\overline{D}\,\frac{\partial m_1}{\partial x_k}\right)\right]} \\
&\quad -\overline{D}\,\overline{\left(\frac{\partial m_1''}{\partial x_j}\right)^2\frac{\partial}{\partial x_k}(\rho\,u_k)} \\
&= -2\,\overline{D}\,\overline{\rho\,\frac{\partial m_1''}{\partial x_j}\,\frac{\partial m_1''}{\partial x_k}}\,\frac{\partial \widetilde{u}_k}{\partial x_j} - 2\,\overline{D}\,\overline{\rho\,\frac{\partial m_1''}{\partial x_j}\,\frac{\partial^2 m_1''}{\partial x_j \partial x_k}\,u_k} - 2\,\overline{D}\,\overline{\rho\,\frac{\partial m_1''}{\partial x_j}\,\frac{\partial u_k''}{\partial x_j}}\,\frac{\partial \widetilde{m}_1}{\partial x_k} \\
&\quad -2\,\overline{D}\,\overline{\rho\,\frac{\partial m_1''}{\partial x_j}\,u_k''}\,\frac{\partial^2 \widetilde{m}_1}{\partial x_j \partial x_k} - 2\,\overline{D}\,\overline{\rho\,\frac{\partial m_1''}{\partial x_j}\,\frac{\partial m_1''}{\partial x_k}\,\frac{\partial u_k''}{\partial x_j}} \\
&\quad +2\,\overline{D}\,\overline{\rho\,\frac{\partial m_1''}{\partial x_j}\,\frac{\partial}{\partial x_j}\left[\frac{1}{\rho}\,\frac{\partial}{\partial x_k}\left(\rho\,\overline{D}\,\frac{\partial m_1}{\partial x_k}\right)\right]} - \overline{D}\,\overline{\left(\frac{\partial m_1''}{\partial x_j}\right)^2\frac{\partial}{\partial x_k}(\rho\,u_k)}\,.
\end{aligned}$$

Using the approximations $\frac{\partial}{\partial x_k}\left(\rho D \frac{\partial m_1}{\partial x_k}\right) \approx \rho D \nabla^2 m_1$ (valid for this flow as ρ is very close to unity) and $\partial^2 \widetilde{m}_1/\partial x_j \partial x_k \approx 0$, and the identities

$$\overline{\rho\,\frac{\partial m_1''}{\partial x_j}\,\frac{\partial^2 m_1''}{\partial x_j \partial x_k}\,u_k} = \frac{1}{2}\,\frac{\partial}{\partial x_k}\left[\overline{\rho\left(\frac{\partial m_1''}{\partial x_j}\right)^2 u_k}\right] - \frac{1}{2}\,\overline{\left(\frac{\partial m_1''}{\partial x_j}\right)^2\frac{\partial}{\partial x_k}(\rho\,u_k)}\,,$$

$$\begin{aligned}
\overline{\rho\,\frac{\partial m_1''}{\partial x_j}\,\frac{\partial}{\partial x_j}\left[\frac{1}{\rho}\,\frac{\partial}{\partial x_k}\left(\rho\,D\,\frac{\partial m_1}{\partial x_k}\right)\right]} &\approx \overline{\rho\,D\,\frac{\partial m_1''}{\partial x_j}\,\frac{\partial}{\partial x_j}(\nabla^2 m_1)} \\
&\approx \frac{\partial}{\partial x_k}\left(\overline{\rho\,D\,\frac{\partial m_1''}{\partial x_j}\,\frac{\partial^2 m_1}{\partial x_j \partial x_k}}\right) - \overline{\rho\,D\,\frac{\partial^2 m_1''}{\partial x_j \partial x_k}\,\frac{\partial^2 m_1}{\partial x_j \partial x_k}} \\
&\approx \frac{1}{2}\,\nabla^2\left[\overline{\rho\,D\left(\frac{\partial m_1''}{\partial x_j}\right)^2}\right] - \overline{\rho\,D\left(\frac{\partial^2 m_1''}{\partial x_j \partial x_k}\right)^2}
\end{aligned}$$

then gives Eq. (22).

[1] N. J. Mueschke and O. Schilling, "Investigation of Rayleigh–Taylor turbulence and mixing using direct numerical simulation with experimentally measured initial conditions. I. Comparison to experimental data," Phys. Fluids **21**, 014106 (2009).

[2] D. M. Snider and M. J. Andrews, "Rayleigh–Taylor and shear driven mixing with an unstable thermal stratification," Phys. Fluids **6**, 3324 (1994).

[3] P. N. Wilson and M. J. Andrews, "Spectral measurements of Rayleigh–Taylor mixing at small Atwood num-

ber," Phys. Fluids **14**, 938 (2002).

[4] P. Ramaprabhu and M. J. Andrews, "Simultaneous measurements of velocity and density in buoyancy-driven mixing," Exp. Fluids **34**, 98 (2003).

[5] P. Ramaprabhu and M. J. Andrews, "Experimental investigation of Rayleigh–Taylor mixing at small Atwood numbers," J. Fluid Mech. **502**, 233 (2004).

[6] N. J. Mueschke, M. J. Andrews, and O. Schilling, "Experimental characterization of initial conditions and spatio-temporal evolution of a small-Atwood-number Rayleigh–Taylor mixing layer," J. Fluid Mech. **567**, 27 (2006).

[7] N. J. Mueschke, "Experimental and numerical study of molecular mixing dynamics in Rayleigh–Taylor unstable flows," Ph.D. thesis, Texas A&M University (2008).

[8] N. J. Mueschke, O. Schilling, D. L. Youngs, and M. J. Andrews, "Measurements of molecular mixing in a high Schmidt number Rayleigh–Taylor mixing layer," J. Fluid Mech. **632**, 17 (2009).

[9] A. Banerjee and M. J. Andrews, "Statistically steady measurements of Rayleigh–Taylor mixing in a gas channel," Phys. Fluids **18**, 035107 (2006).

[10] W. N. Kraft, "Simultaneous and instantaneous measurement of velocity and density in Rayleigh–Taylor mixing layers," Ph.D. thesis, Texas A&M University (2008).

[11] N. J. Mueschke and O. Schilling, "Investigation of Rayleigh–Taylor turbulence and mixing using direct numerical simulation with experimentally measured initial conditions. II. Dynamics of transitional flow and mixing statistics," Phys. Fluids **21**, 014107 (2009).

[12] A. W. Cook and P. E. Dimotakis, "Transition stages of Rayleigh–Taylor instability between miscible fluids," J. Fluid Mech. **443**, 69 (2001). Corrigendum, J. Fluid Mech. **457**, 410 (2002).

[13] J. R. Ristorcelli and T. T. Clark, "Rayleigh–Taylor turbulence: self-similar analysis and direct numerical simulations," J. Fluid Mech. **507**, 213 (2004).

[14] P. Chassaing, "The modeling of variable density turbulent flows," Annu. Rev. Fluid Mech. **66**, 293 (2001).

[15] J. Boussinesq, *Theorie Analytique de la Chaleur Vol. 2*, (Gauthier-Villars, Paris, 1903).

[16] W. S. Cleveland and S. J. Devlin, "Locally weighted regression: an approach to regression analysis by local fitting," J. Amer. Stat. Assoc. **83**, 596 (1988).

[17] S. Chandrasekhar, *Hydrodynamic and Hydromagnetic Stability*, (Dover, New York, 1961).

[18] P. Chassaing, R. A. Antonia, F. Anselmet, L. Joly, and S. Sarkar, *Variable Density Fluid Turbulence*, Fluid Mechanics and its Applications Vol. 69, (Kluwer Academic, Amsterdam, 2002).

[19] S. B. Pope, *Turbulent Flows* (Cambridge University Press, New York, 2000).

[20] D. L. Youngs, "Numerical simulation of mixing by Rayleigh–Taylor and Richtmyer–Meshkov instabilities," Laser Part. Beams **12**, 725 (1994).

[21] P. Ramaprabhu, G. Dimonte, and M. J. Andrews, "A numerical study of the influence of initial perturbations on the turbulent Rayleigh–Taylor instability," J. Fluid Mech. **536**, 285 (2005).

[22] W. H. Cabot and A. W. Cook, "Reynolds number effects on Rayleigh–Taylor instability with implications for type Ia supernovae," Nat. Phys. **2**, 562 (2006).

[23] D. D. Joseph, "Fluid dynamics of two miscible liquids with diffusion and gradient stress," Eur. J. Mech. B/Fluids **9**, 565 (1990).

[24] W. H. Cabot, O. Schilling, and Y. Zhou, "Influence of subgrid scales on resolvable turbulence and mixing in Rayleigh–Taylor flow," Phys. Fluids **16**, 495 (2004).

[25] S. Jakirlić and K. Hanjalić, "A new approach to modelling near-wall turbulence energy and stress dissipation," J. Fluid Mech. **459**, 139 (2002).

[26] N. N. Mansour, J. Kim, and P. Moin, "Reynolds-stress and dissipation rate budgets in a turbulent channel flow," J. Fluid Mech. **194**, 15 (1988).

[27] C.-J. Chen and S.-Y. Jaw, *Fundamentals of Turbulence Modeling*, Combustion: An International Series (Taylor and Francis, 1998).

[28] R. O. Fox, *Computational Models for Turbulent Reacting Flows*, Cambridge Series in Chemical Engineering (Cambridge University Press, Cambridge, 2003).

[29] H. Tennekes and J. L. Lumley, *A First Course in Turbulence* (MIT Press, Cambridge, 1972).

[30] D. Veynante and L. Vervisch, "Turbulent combustion modeling," Prog. Energy and Combust. Sci. **28**, 193 (2002).

[31] T. Poinsot and D. Veynante, *Theoretical and Numerical Combustion*, second edition (R. T. Edwards, 2005).

[32] N. Peters, *Turbulent Combustion*, Cambridge Monographs on Mechanics (Cambridge University Press, Cambridge, 2000).

[33] T. Mantel and R. Borghi, "A new model of premixed wrinkled flame propagation based on a scalar dissipation equation," Combust. and Flame **96**, 443 (1994).

[34] A. Mura and R. Borghi, "Towards an extended scalar dissipation equation for turbulent premixed combustion," Combust. and Flame **133**, 193 (2003).

[35] A. Mura, V. Robin, and M. Champion, "Modeling of scalar dissipation in partially premixed turbulent flames," Combust. and Flame **149**, 217 (2007).

[36] W. P. Jones and B. E. Launder, "The prediction of laminarization with a two-equation model of turbulence," Int. J. Heat and Mass Transfer **15**, 301 (1972); W. P. Jones and B. E. Launder, "Erratum: The prediction of laminarization with a two-equation model of turbulence," *ibid.* **16**, 2128 (1973).

[37] M. M. Rogers and P. Moin, "The structure of the vorticity field in homogeneous turbulent flows," J. Fluid Mech. **176**, 33 (1987).

[38] S. Tavoularis and S. Corrsin, "Experiments in nearly homogeneous turbulent shear flow with a uniform mean temperature gradient. Part 1," J. Fluid Mech. **104**, 311 (1981).

[39] M. M. Rogers and R. D. Moser, "Direct simulation of a self-similar turbulent mixing layer," Phys. Fluids **6**, 903 (1994).

[40] J. P. Mellado, S. Sarkar, and Y. Zhou, "Large-eddy simulation of Rayleigh–Taylor turbulence with compressible miscible fluids," Phys. Fluids **17**, 076101 (2005).

[41] P. Bradshaw, "Turbulence - the chief outstanding difficulty of our subject," Exp. Fluids **16**, 203 (1994).

[42] R. Schiestel, *Modeling and Simulation of Turbulent Flows* (Wiley, New York, 2008).

Prepared by LLNL under Contract DE-AC52-07NA27344